Synchronizing clocks via satellites using entangled photons: Effect of relative velocity on precision

Stav Haldar ●,[1,*] Ivan Agullo,[1] and James E. Troupe[2]

[1]*Department of Physics & Astronomy, Louisiana State University, Baton Rouge, Louisiana 70803, USA*

[2]*Xairos Systems, Inc., Denver, Colorado 80124, USA*

A satellite-based scheme to perform clock synchronization between ground stations spread across the globe using quantum resources was proposed in [Phys. Rev. A **107**, 022615 (2023).] based on a quantum clock synchronization (QCS) protocol. Such a scheme could achieve synchronization up to the picosecond level over distances of thousands of kilometers. Nonetheless, the implementation of this QCS protocol has yet to be demonstrated experimentally in situations where the satellite velocities cannot be neglected, as is the case in many realistic scenarios. In this work, we develop analytical and numerical tools to study the effect of the relative velocity between the satellite and ground stations on the success of the QCS protocol. We conclude that the protocol can still run successfully if the data-acquisition window is chosen appropriately. As a demonstration, we simulate the synchronization outcomes for cities across the continental United States using a single satellite in a low earth orbit, low-cost entanglement sources, portable atomic clocks, and avalanche detectors. We conclude that, after including the effect of relative motion, subnanosecond- to picosecond-level precision can still be achieved over distance scales of $\approx$4000 km. Such high-precision synchronization is currently not achievable over long distances ($\gtrsim$100 km) with standard classical techniques including the GPS. The simulation tools developed in this work are in principle applicable to other means of synchronizing clocks using entangled photons, which are expected to form the basis of future quantum networks like the quantum internet, distributed quantum sensing, and the quantum GPS.

I. INTRODUCTION

A satellite-based quantum clock synchronization (QCS) scheme for time distribution among a network of ground based clocks was introduced in Ref. [1]. We concluded that such a QCS scheme could achieve subnanosecond precision at the global scale utilizing modest optical sources, modestly stable clocks, and a small constellation of low earth orbit (LEO) satellites. In this scheme, establishment of elementary links between satellite and individual ground stations is achieved via the exchange of entangled photons and, subsequently, the satellites act as intermediaries for synchronizing different ground stations. This scheme is based on the QCS protocol introduced in Ref. [2], which has been experimentally demonstrated to achieve picosecond sync level precision between stationary clocks on Earth with as few as 20 detected entangled photon pairs [3] (for a more recent demonstration also see Ref. [4]).

Given the large number of variables involved when moving satellites are considered, our previous analysis in Ref. [1] was performed under some simplifying assumptions. The main one was to use the rate of exchange of entangled photons between satellites and ground stations as a proxy for the precision at which they can synchronize—rather than a detailed calculation of the correlation functions involved in the protocol, which ultimately determine the sync precision. This

assumption was backed by numerical simulations and allowed us to focus attention on kinematic aspects involving losses, beam spreading, sync area coverage, etc. In this work, we go a step beyond and quantitatively analyze the effects of the relative instantaneous velocities on the performance of the protocol, quantifying the way relative motion limits the sync precision and determining the optimal data-acquisition time. The main assumption was that if the rate of exchange of entangled photons in the elementary link is greater than a cutoff, the QCS protocol succeeds at a certain precision. This assumption, although backed by static simulations, fails to hold in the dynamic picture, where the precision of the QCS protocol is effected by the relative motion between the satellite and the ground station (gs). The present work determines the degree at which the QCS protocol, which has successfully tested to synchronize stationary clocks, can be generalized to moving clocks and hence to space-based applications, which have shown great promise in extending the scale and efficiency of quantum networks [5,6].

The main goal of this paper is thus to assess the feasibility of a QCS network by determining the achievable precision, network scale, and connectivity, primarily in terms of the performance of the elementary links.

Our analysis has applicability beyond the concrete QCS protocol analyzed in this article, in particular to the protocols based on distributing entanglement from moving satellites [5,6], an application that we explore in a separate presentation.

Before describing our methods and results, it is important to briefly motivate (a) the need for a QCS network and (b) the

_____
*hstav1@lsu.edu

advantages of using entangled photons and a constellation of satellites to establish such a network of synchronized clocks.

The ability to measure, hold and distribute time at high precision determines the limits of our scientific explorations. From a technological point of view, precise time measurement and synchronization is an indispensable feature of communication and networking protocols, navigation and ranging, astronomical, geological and meteorological measurements, among others [5,7–10]. It must be further stressed that most realizations of quantum protocols such as teleportation and quantum key distribution have an inherent requirement for continuous, high-accuracy clock synchronization at the sub-nanosecond level [11,12]. Tremendous advances have been made in classical techniques for clock synchronization [13], for example, using radiofrequency pulses [14] and optical frequency combs [15]. Although these techniques can provide synchronization in the picosecond to femtosecond range, considerable challenges exist in their long distance (>100 km) implementations, such as large computational overhead and transfer of technology to satellite payloads [13,15]. It is thus important to look at QCS networks from the perspective of complementing these state-of-the-art synchronization and time distribution protocols for long-distance applications. At the same time, we also point out new application spaces for QCS networks, given the inherent advantages of quantum communication over classical communication [16–29].

Quantum state transfer protocols such as teleportation and key distribution have been carried out over continental distances of more than 1000 km [16,30–32]. To contrast with the limits of fiber-optic-based quantum communication, we note that the quantum repeater-less fiber-optic-based secret key rate bound is surpassed beyond 215 km for a satellite at an altitude of 530 km [5,16]. A key role in developing feasible long-distance quantum communication implementations has thus been played by the transition to hybrid space-terrestrial quantum communication network architectures [32–34]. This combines satellites and ground stations equipped with optical telescopes with metropolitan-scale fiber-optic networks. This is because large-scale realizations of fully terrestrial quantum networks are hindered by the exponential losses associated with ground-based communication channels (primarily fiber-optic cables) [6]. Large numbers of high-fidelity quantum repeaters and/or quantum memories could improve the situation to some extent, but their current performance levels are below those needed for mature applications [5], and furthermore, it would very likely be impractical to place such devices in difficult terrain, e.g., mountains or oceans.

Finally, we justify the use of incoherent optical communication (single-photon detection) via entangled photons for distributing time, when the same can be achieved classically. Subnanosecond synchronization is currently not easily achievable over long distances because GPS only allows synchronization with a precision of >40 nanoseconds (95% of the time). Furthermore, for very long optical links with high loss, e.g., those between LEO satellites and ground stations, high-precision synchronization will have to be achieved with a relatively small number of received photons. In this regard, it is important to point out that optical communication techniques that use single-photon detection (noncoherent or

quantum measurement) have a provable advantage in terms of power efficiency (bits per photon) over the coherent optical communication techniques which are generally used in high-precision, classical-optics-based clock synchronization, e.g., classical O-TWTFT [35]. As mentioned earlier, picosecond-level QCS was demonstrated in a ground based setting to work with as few as 20 detected entangled photons. This makes it an ideal candidate for high-loss satellite-based quantum communication channels.

The structure of the paper is as follows: In Sec. II, we describe the QCS protocol and find analytical results for the achievable precision and network scale. We consider the effects of relative motion between clocks (range-rate change), channel loss, and background noise. In Sec. IV, we provide details about the simulation techniques used, and in Secs. V and VI, we present the results of these simulations, developing tools to assess and describe the QCS network outcomes. More specifically, in Sec. VI we show that, for a QCS network of four cities—New York, Atlanta, Los Angeles, and Seattle—subnanosecond- to picosecond-level clock sync precision can be achieved by using modest resources. We present our conclusions and directions for future work in Sec. VII.

II. DESCRIPTION OF THE PROTOCOL

We briefly describe a QCS protocol to remotely synchronize a network of clocks located on the Earth using satellites in Earth orbits as intermediaries. The main resource used in the protocol is time-correlated photons generated out of a spontaneous parametric down conversion (SPDC) source. As an added advantage, the entanglement or quantum correlations in the polarization degree of freedom can be utilized to enhance the security of the protocol. For more details on the security analysis and experimental implementation, we point the reader to foundational work on this protocol [2,3]. To begin the discussion, we describe a simpler scenario which is entirely ground based and involves stationary clocks, to familiarize ourselves with the cogs and wheels of the protocol. This would make the subsequent discussion of the satellite-based version involving moving clocks cogent.

A. Ground-based protocol

Consider two clocks at A and B with Alice and Bob, which are assumed to have the same frequency within the precision of the synchronization task and are stable enough to maintain this frequency during the time in which the sync protocol is executed—we discuss below how to relax this assumption. Now, consider that they have a constant offset of Δ. The task of the protocol is to find the value of Δ. Say B is ahead of A. Consider that both Alice and Bob have an SPDC source to generate entangled photon pairs. Alice generates a pair at a random time t_a; one photon from the pair is locally detected and timestamped by Alice; the other photon travels to Bob and is detected and timestamped at time t_b, using a single-photon detector. If t_{ab} is the travel time for the photon between A and B then,

$$t_b' = t_a + t_{ab} + \Delta. \tag{1}$$

Similarly, for a photon pair generated at Bob's end and detected at A:

$$t_a = t'_b + t_{ba} - \Delta. \qquad (2)$$

Consider the distributions $A(t)$ and $B(t)$ which count the photon detection events at A and B, respectively,

$$A(t) = \Sigma_i \delta\big(t - t_a^i\big). \qquad (3)$$

Similarly, for photons detected by Bob

$$B(t') = \Sigma_j \delta\big(t' - t_b'^{j}\big). \qquad (4)$$

Finally, consider the time-stamp cross-correlation function for these detection events, $C_{AB}(\tau)$, defined as

$$C_{AB}(\tau) = \int_0^{t_{\mathrm{Acq}}} A(t)B(t+\tau)dt. \qquad (5)$$

Here, the acquisition time t_{Acq} is the total time for which the protocol runs, i.e., photon detection timestamps collected over a time window t_{Acq} are used to find the cross-correlation functions. We later show that the choice of t_{Acq} plays an important role in the success of the QCS protocol. Using Equations (1)–(4), it is easy to see that $C_{AB}(\tau)$ has a peak at

$$\tau_{\mathrm{max}}^{ab} = t_{ab} + \Delta. \qquad (6)$$

A similarly defined correlation function

$$C_{BA}(\tau) = \int_0^{t_{\mathrm{Acq}}} B(t')A(t'+\tau)dt' \qquad (7)$$

has a peak at

$$\tau_{\mathrm{max}}^{ba} = t_{ba} - \Delta. \qquad (8)$$

If we assume reciprocity of the time of travel [2,36], i.e., $t_{ab} = t_{ba}$, adding and subtracting Eqs. (6) and (8) we get the time of travel and the offset as

$$\Delta = \frac{\tau_{\mathrm{max}}^{ab} - \tau_{\mathrm{max}}^{ba}}{2}, \qquad (9)$$

$$t_{ab} = t_{ba} = \frac{\tau_{\mathrm{max}}^{ab} + \tau_{\mathrm{max}}^{ba}}{2}. \qquad (10)$$

So, looking at the peaks of these two-way correlation functions, both the time of travel (9) and the offset (10) can be evaluated (see Fig. 1 for an example). It is noteworthy that, although an entanglement source is used to produce the photons that are then timestamped for the QCS protocol, the polarization degree of freedom which has the quantum correlations is never invoked. The protocol only relies on the tight time-correlations between such photons. Therefore, the quantumness of the protocol comes from the use of single-photon sources and detectors and the randomness of the time of birth of the SPDC photon pairs. The entanglement between photons is not explicitly used, although it can play an important role in adding an extra layer of security to the protocol.

Some effects which can deteriorate the success rate and precision of this protocol include channel loss, dark counts, and background noise. Furthermore, since here we limit ourselves to determining a fixed offset between the two clocks, any relative frequency differences and/or drifts lead to spreading of the cross-correlation function peaks. This effect is very similar to relative motion between the clocks changing the
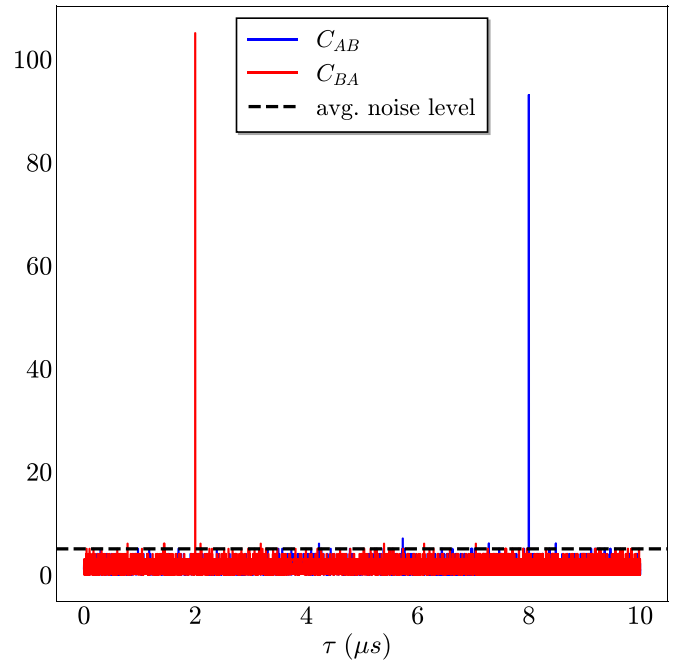
FIG. 1. Here, we show the timestamp cross-correlation functions obtained via a Monte Carlo simulation of the QCS protocol. The effects of channel loss, noise, and dark counts have been included. The average noise level shown is a rough guide to eye to show the height the genuine peaks must surpass in order for the protocol to be successful (signal-to-noise ratio). The background noise + dark count combined rate is assumed to be 10^7 photons/s, the source rate is also 10^7 ebits/s. The channel loss is 20 dB (representative of an uplink between a ground station and a polar satellite when the satellite is overhead the ground station). We have chosen $t_{\mathrm{Acq}} = 1$ ms in this plot. The offset between the clocks has been chosen to be 6 μs; this number can be correctly obtained from the figure as the gap between the two peaks. The least count of the timestamps is 0.5 ns. Since we have two unique peaks in this case, the offset can thus be determined at this precision (0.5 ns).

time of travel between the two. This is the main challenge we seek to address in this work and we begin a detailed discussion in the next section. For effects of frequency differences and drifts see also Refs. [3,4,37].

Finally, we make a short comment about classical communication and computational times. Both these tasks can be performed after the quantum part of the protocol is complete. Say the satellite and ground station clocks share the required number of ebits for the success of QCS. The sharing of the timestamps by the two parties can be done later using classical signals, as long as there is visibility. As will be shown in Sec. IV, the required quantum data-acquisitions times are of the order of a few milliseconds, or even less, and the visibility periods for an LEO satellite over a given point on Earth is roughly a few 100 seconds, providing more than ample time for classical communication. In fact, multiple attempts for quantum clock synchronization can be made within this visibility period, even after accounting for classical communication times. Furthermore, the computation of correlation functions can be performed (if needed using multiple cores in

parallel and at the ground station) when the two parties are no longer visible to each other.

B. Challenges for a satellite based version of the protocol: How to synchronize clocks in relative motion?

Consider now that Alice and Bob are separated in a way that makes it inefficient to exchange photons directly between the two parties. A quantum network between different cities is an example of such a scenario. The distances are large enough (≈ 1000 km) to make direct communication through standard optical fiber channels (even with repeaters) less efficient and resource consuming than communication through a network of intermediary satellites in low Earth orbits. The satellites are to be used as intermediaries in the sense that ground station A can be synced to a satellite and then the same satellite could be synced to the ground station B. If all three clocks involved are relatively stable within the time this protocol is executed then the clocks at A and B can be successfully synced in this way. Consider now the elementary link or task of this protocol, which is to sync a ground station to a satellite. The roles of Alice and Bob are thus taken up by the ground station and satellite, respectively. The main difference between the task in the ground-based case and this satellite-based case is the relative motion between the clocks that need to be synchronized. Satellite velocities in LEOs can be of the order of a few kilometers per second with respect to the ground stations. Throughout this work we will assume circular orbits for satellites (and ground stations). Therefore, the link distance, which is now a function of time, changes by Δd_{ab} in time t, given by

$$\Delta d_{ab}(t) = v_{\text{rel}}^{\text{rad}} t, \tag{11}$$

where $v_{\text{rel}}^{\text{rad}}$ is the relative radial velocity of the satellite with respect to the ground station and is given in terms of the position vectors $\mathbf{r}_{\text{sat}}$, $\mathbf{r}_{\mathbf{gs}}$ (with respect to the center of the Earth), and angular velocities ω_{sat}, $\omega_{\mathbf{gs}}$ of the satellite and ground station, respectively:

$$v_{\text{rel}}^{\text{rad}} = (\mathbf{r}_{\text{sat}} \times \omega_{\text{sat}} - \mathbf{r}_{\mathbf{gs}} \times \omega_{\mathbf{gs}}).\frac{(\mathbf{r}_{\text{sat}} - \mathbf{r}_{\mathbf{gs}})}{|(\mathbf{r}_{\text{sat}} - \mathbf{r}_{\mathbf{gs}})|}. \tag{12}$$

Thus, the time of travel for a photon moving between A and B also becomes a function of time given by

$$t_{ab}(t) = \frac{d_{ab}(t)}{c}, \tag{13}$$

where c is the speed of light in vacuum (we are ignoring the small variation in the speed of light when it enters the atmosphere, since the thickness of the atmosphere is ≈ 10 km $\ll$ d_{ab}). Assuming a small enough acquisition time t_{Acq} such that the relative radial velocity does not change appreciably within the precision levels of the protocol and also any relativistic effects can be ignored, during the interval t_{Acq} the time of

travel changes by Δt_{ab} given by[1]

$$\Delta t_{ab} = \frac{\Delta d_{ab}(t_{\text{Acq}})}{c}, \tag{14}$$

When looked at in conjugation with Eqs. (6) and (8), this tells us that the correlation function no longer has a single sharp peak. New peaks keep on appearing adjacent to the first peak as the time of travel changes with time, forming a broad band. The correlation function has, therefore, multiple adjacent peaks given by the modified form of Eq. (6):

$$\tau_{ab}(t) = t_{ab}(t) + \Delta. \tag{15}$$

Now, the pertinent question is how can a unique and accurate value of the time offset Δ be evaluated, up to a certain precision, given these new features of the correlation function C_{AB}?

In the rest of the paper we take a two-pronged approach. First of all, we define and analytically calculate the signal-to-noise ratio (SNR) of the timestamp correlation functions and define from it the achievable precision. Second, we perform Monte Carlo simulations of the QCS protocol, and, finally, we combine the intuition gained by the Monte Carlo simulations and analytical results to perform numerical simulations for a full QCS network to calculate figures of merit, taking into account the motion of multiple satellites and ground stations and the dynamics of lossy channels between them.

III. BEHAVIOR OF THE CORRELATION FUNCTIONS

The success and precision of the protocol depends on the sharpness of the correlation function peak. This sharpness can be quantified through the signal-to-noise ratio (SNR), defined as the quotient of the height of the peak above the average noise level (spurious peaks) and the standard deviation of the noise (see Appendix B). For simplicity of notation, we now drop the indices A and B, since the analysis applies equally to both correlation functions.

The height of the peak in C if the two parties were stationary is given by

$$C(\tau_{\max}) = R \eta t_{\text{Acq}}, \tag{16}$$

where R is the source rate, at which the entangled photons are produced, and η is the probability of detection at the receiver's end. η includes the efficiency of the detectors as well as the effects of losses in the propagation. Hence, η depends on the distance between the two parties. For more details on the loss model, we refer the reader to Appendix A and Ref. [6]. Succinctly stated here, the transmissivity η has three factors:

i. Free-space transmittance: This includes effects of beam broadening and finite apertures of the transmitting and receiving telescopes.

ii. Atmospheric transmittance: we assume the atmosphere to be a homogeneous absorptive medium following the Beer-Lambert law (transmittance falls exponentially

---

[1]For the GPS, the combined special and general relativistic effects are ≈ 0.5 ns/s [38]. We see in Sec. V that the optimal acquisition time is in the submillisecond range, which means relativistic effects only become important when the precision required is in the subpicosecond range.

with increasing distance that is traveled through the medium).

iii. Detector inefficiencies: κ_{sat} and κ_{grd} are efficiencies of the detectors at the satellite and ground station, respectively.

Thus, the total efficiency of the channel (uplink or downlink) is given by $\eta = \eta_{\text{atm}}\eta_{\text{fs}}\kappa_{\text{sat}}\kappa_{\text{grd}}$. Finally, it is important to note that, when relative motion is not considered, Eq. (16) shows that the height $C(\tau_{\text{max}})$ keeps on increasing with the acquisition time t_{Acq}.

On the other hand, this is no longer true in the case with relative motion (see Fig. 2). The height of a peak only rises until the time of travel t_{ab} changes by unit precision. Let t_{bin} be the maximum achievable precision (least count or bin size for timestamps in the simulation). In that case, the peak in $C(\tau_{\text{max}})$ due to correlated photons rises only until the acquisition time reaches the value $t_{\text{Acq}}^{\text{opt}}$ given by the following condition:

$$\Delta t_{ab}(t_{\text{Acq}}^{\text{opt}}) = t_{\text{bin}}. \tag{17}$$

After $t_{\text{Acq}}^{\text{opt}}$, a new peak starts rising, adjacent to the first peak. (The reason for referring to this as the optimal acquisition time will become obvious later in this section.) Using Eqs. (11) and (14) in (17), we can obtain the value of $t_{\text{Acq}}^{\text{opt}}$ in terms of other parameters:

$$t_{\text{Acq}}^{\text{opt}} = \mathcal{K} t_{\text{bin}}, \tag{18}$$

where the geometrical factor $\mathcal{K}$ is given by $\mathcal{K} = c/v_{\text{rel}}^{\text{rad}}$; $\mathcal{K}$ depends, via v_{rel}, on the distance between A and B; this will be important shortly.

Therefore, $t_{\text{Acq}}^{\text{opt}}$ quantifies the acquisition time at which the position of the peak in the correlation function shifts by one unit precision t_{bin}, from τ_{max} to $\tau_{\text{max}} + t_{\text{bin}}$. In turn, this determines the maximum height of any peak generated by true correlations, which is given by

$$C(\tau_{\text{max}}) = R \, \eta \mathcal{K} t_{\text{bin}}. \tag{19}$$

Clearly, the SNR will have different behaviors for the two regimes defined by $t_{\text{Acq}} < t_{\text{Acq}}^{\text{opt}}$ and $t_{\text{Acq}} > t_{\text{Acq}}^{\text{opt}}$. We derive the SNR for these two regimes in the Appendix B. Assuming that photons from background noise appear at a rate R_{bkg}, we obtain the following expressions for the SNR:

i. For $t_{\text{Acq}} < t_{\text{Acq}}^{\text{opt}}$,

$$\text{SNR} \approx \sqrt{\frac{\eta}{t_{\text{bin}}(1 + R_{\text{bkg}}/R\eta)}} \sqrt{t_{\text{Acq}}}. \tag{20}$$

Therefore, for $t_{\text{Acq}} < t_{\text{Acq}}^{\text{opt}}$ the SNR increases with the acquisition time as $\sqrt{t_{\text{Acq}}}$. This is due to the fact that, for $t_{\text{Acq}} < t_{\text{Acq}}^{\text{opt}}$, the height of the peak grows faster than the noise.

ii. For $t_{\text{Acq}} > t_{\text{Acq}}^{\text{opt}}$,

$$\text{SNR} \approx \mathcal{K}\sqrt{\frac{\eta t_{\text{bin}}}{\sqrt{(1 + R_{\text{bkg}}/R\eta)}}} \frac{1}{\sqrt{t_{\text{Acq}}}}. \tag{21}$$

Therefore, for $t_{\text{Acq}} > t_{\text{Acq}}^{\text{opt}}$, the SNR decreases with increasing t_{Acq}. Again, this is expected because in this regime the height of the peak no longer increases, while noise keeps accumulating.
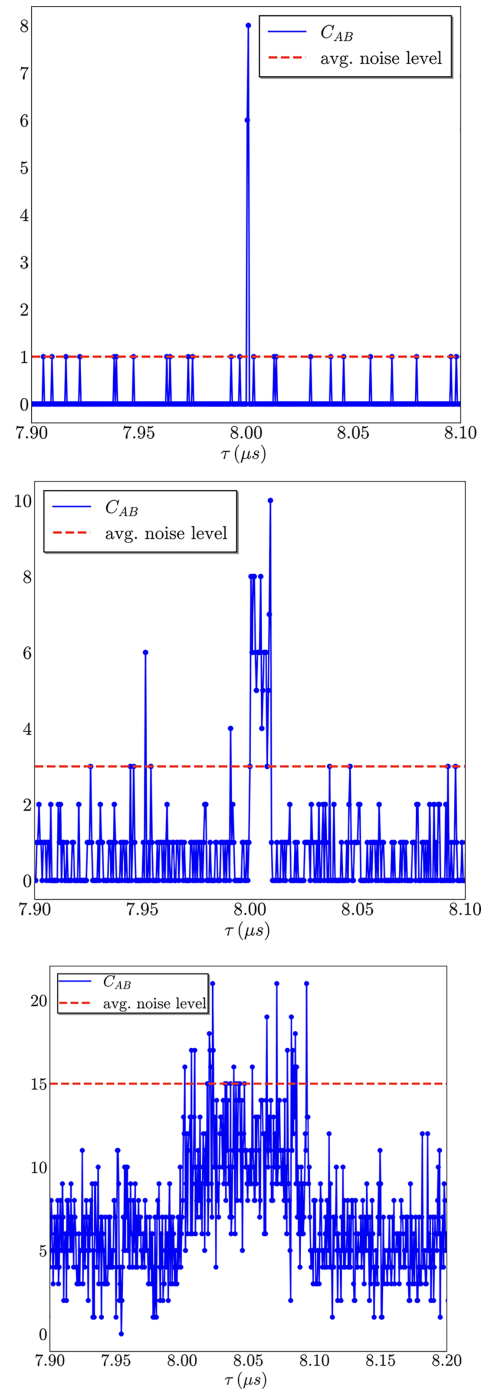
FIG. 2. Here, we show the timestamp cross-correlation functions obtained via a Monte Carlo simulation of the QCS protocol between two clocks in relative motion (one on a satellite and one on ground station). As the acquisition time increases from 0.1 ms in the topmost plot to 1 ms in the center, and finally 10 ms on the bottom plot, multiple peaks start appearing due changes in the time of travel, i.e., the peak broadens. The gap between peaks and average noise level (indicated by the red dotted line as a guide to the eye) reduces with increasing t_{Acq}, reducing the SNR of the true peaks. The background noise rate is 10^6 photons/s and source rate is 10^7 ebits/s. The channel loss is around 20 dB (uplink loss between a ground station and a polar satellite at 500 km altitude varies slightly because the satellite and ground station both move during the acquisition time). Least count is 0.5 ns.

This analysis clearly indicates that the SNR is maximum for $t_{Acq} = t_{Acq}^{opt}$. Its maximum value is

$$\text{SNR}_{\max} \approx \sqrt{\frac{\eta \mathcal{K}}{(1 + R_{bkg}/R\eta)}}. \quad (22)$$

On the other hand, in order to get a clearly defined peak recognizable out of the noise, the SNR must be greater than a threshold SNR_{th}. The higher our choice for this threshold is, the lower is the probability of misidentifying a peak. For a choice of SNR_{th}, the condition for a peak to be identifiable is

$$\text{SNR}_{\max} \geqslant \text{SNR}_{th}, \quad \text{or,} \quad \text{equivalently,}$$

$$\sqrt{\frac{\eta \mathcal{K}}{(1 + R_{bkg}/R\eta)}} \geqslant \text{SNR}_{th}. \quad (23)$$

For a given level of background noise, R_{bkg}, the above condition provides a constraint on the relative position of the ground station with respect to the satellite, setting a scale for the service area of the satellite (region on Earth where it can provide synchronization). At the same time, it also puts bounds on the levels of tolerable noise for the sync to be successful for a given configuration of the satellite and ground station positions. Note that this condition does not interfere with sync precision of the protocol, since it is independent of t_{bin}. Furthermore, for simplicity, we have ignored here the effect of detector jitter (which leads to loss of timestamp precision) on the sync precision. We refer the reader to Appendix D for an analysis of these effects.

Apart from the SNR condition just discussed, for a peak in the correlation function to be visible, we must impose an extra requirement on the absolute of the peak's height. This condition comes from the simple fact that one must collect at least a few photons with the correct correlations within the acquisition time; i.e., the peak must have a minimum height. Since the ebit generation through an SPDC source and the losses are both random processes, by setting a minimum threshold for the mean number of ebits detected, we can ensure that at least a few ebits get shared between the ground station and satellite with high probability within the acquisition window. Let $N_{\min}$ be that photon number threshold; if R is the source rate and η the probability of detection, we obtain the following constraint:

$$R\,\eta\,t_{Acq}^{opt} \geqslant N_{\min}. \quad (24)$$

Using Eq. (18), (24) can be rewritten as

$$t_{bin} \geqslant \frac{N_{\min}}{R\eta\mathcal{K}}. \quad (25)$$

Unlike Eq. (23), this constraint involves the sync precision t_{bin}. For a required level of precision, this sets a constraint on the product of geometrical factors η and $\mathcal{K}$, and thus it also defines a scale for the service area of the satellite via the equation:

$$\eta(|\mathbf{r}_{gs} - \mathbf{r}_{sat}|)\mathcal{K}(\mathbf{r}_{gs}, \mathbf{r}_{sat}) \geqslant \frac{N_{\min}}{Rt_{bin}}. \quad (26)$$

For a reasonable value of SNR_{th} and as long as R_{bkg} is not very large (compared with R), Eq. (26) is a stronger condition than Eq. (23) and hence determines the serviceable region (later we call this the precision "shadow" of the satellite). This is the
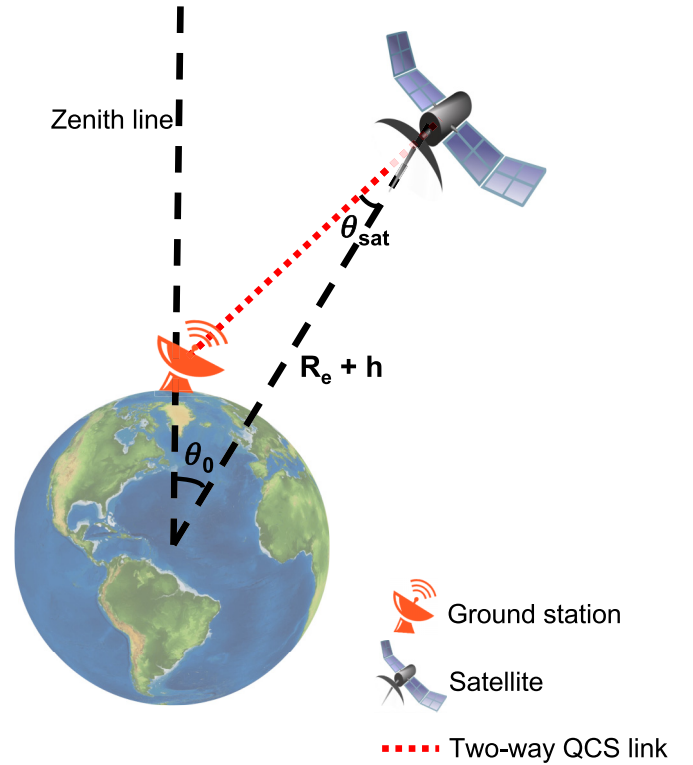
FIG. 3. A simple configuration for the QCS protocol. A satellite orbiting in the plane formed by the two lines joining the center of the Earth to the ground station (zenith line) and to the satellite.

equation we will use later to determine the size of sync networks. Only for very high noise levels may the SNR condition become the dominant constraint on the network size. Finally, we stress that Eq. (25) puts a limit on the achievable precision only when the acquisition time is set to its optimal values. This assumes working at the maximum achievable SNR. The working precision of the protocol could be higher if we loosen this constraint. For more details and an operational view of the protocol, see Appendix C.

A. A simple example

To build some intuition, let us begin by looking at a simple example. Consider a ground station at a random location on Earth's surface. For illustrative purposes, in this example we assume that the line joining the center of the Earth to the ground station (zenith line) lies in the plane defined by the satellite's orbit (Fig. 3). The satellite is at altitude h above the Earth's surface. We assume circular orbit for the satellite and also for the ground station (ignoring any topographical features and the nonspherical geometry of the Earth). R_e is Earth's radius. Say the protocol starts when the satellite makes an angle θ_0 with the zenith. Expressions for $\mathcal{K}$ and SNR can be calculated analytically for this case.

$$\mathcal{K} = \frac{2c\left(R_e^2 + (R_e + h)^2 - 2R_e(R_e + h)\cos\theta_0\right)^{1/2}}{2R_e(R_e + h)\omega\sin\theta_0}. \quad (27)$$

In Eq. (25), on the RHS η and $\mathcal{K}$ depend on the geometrical factors (h, θ_0). Hence, Eq. (25) can be interpreted as the best precision (smallest t_{bin}) that can be achieved at a given relative
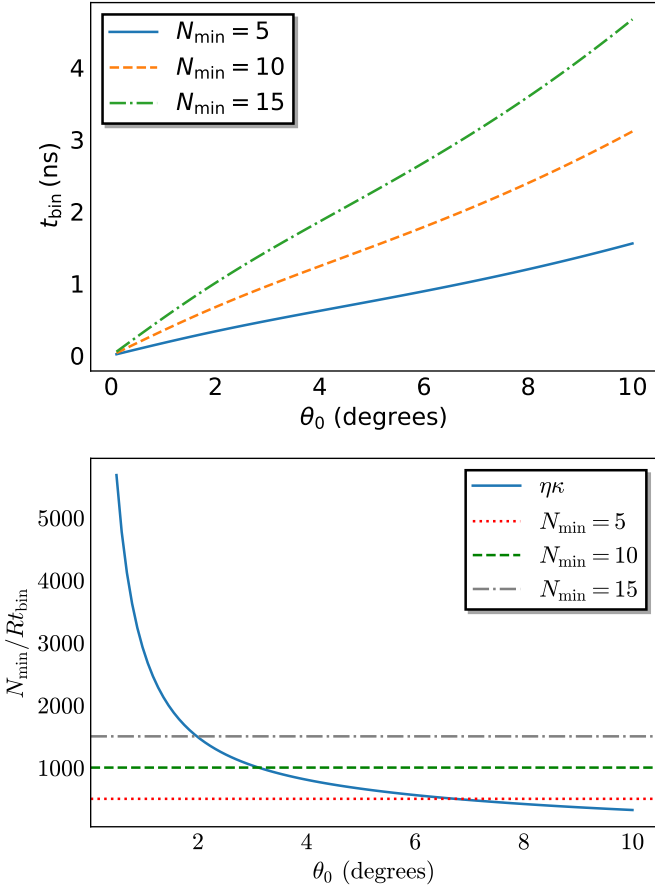
FIG. 4. Two ways of looking at the achievable precision: (top) Maximum achievable precision as a function of the ground station–satellite angular separation, and (bottom) maximum separation allowed (serviceable area) for a required level of precision. θ_0^{crit}, the critical angular separations for 1 ns precision, is given by the intersection of the blue (solid) curve with the horizontal lines (dotted, dashed) corresponding to different choices of $N_{\min}$.

position of the ground station and the satellite. At the same time, from a different point of view, it can be considered as a limit on the relative angular separation between the satellite and ground station up to which a certain precision can be achieved. For example, given a fixed satellite altitude h, the protocol cannot be successfully conducted beyond an angle θ_0^{crit} at a required precision of t_{bin}, where θ_0^{crit} is determined from

$$\eta\big(\theta_0^{\text{crit}}, h\big)\mathcal{K}\big(\theta_0^{\text{crit}}, h\big) \geqslant \frac{N_{\min}}{Rt_{\text{bin}}}. \tag{28}$$

Figure 4 illustrates these two viewpoints looking at the precision. Also, Fig. 5 shows the dependence of SNR on background rates, acquisition time, and angular separation. As a quantitative example, for $h = 500$ km and $N_{\min} = 5$ a precision of $t_{\text{bin}} = 1$ ns can be achieved up to $\theta_0 = \theta_0^{\text{crit}} \approx 3°$, with a source rate of 10^7 ebits/s. This angle, when translated to the coverage angle of the satellite, is $\theta_{\text{sat}} \approx 34°$. That is, all ground stations falling in this angular region will be able to sync with the satellite at 1 ns precision.

As was mentioned in the previous section, even within these limits set by $N_{\min}$, the background noise dictates the SNR and hence it must be low enough such that Eq. (23) is
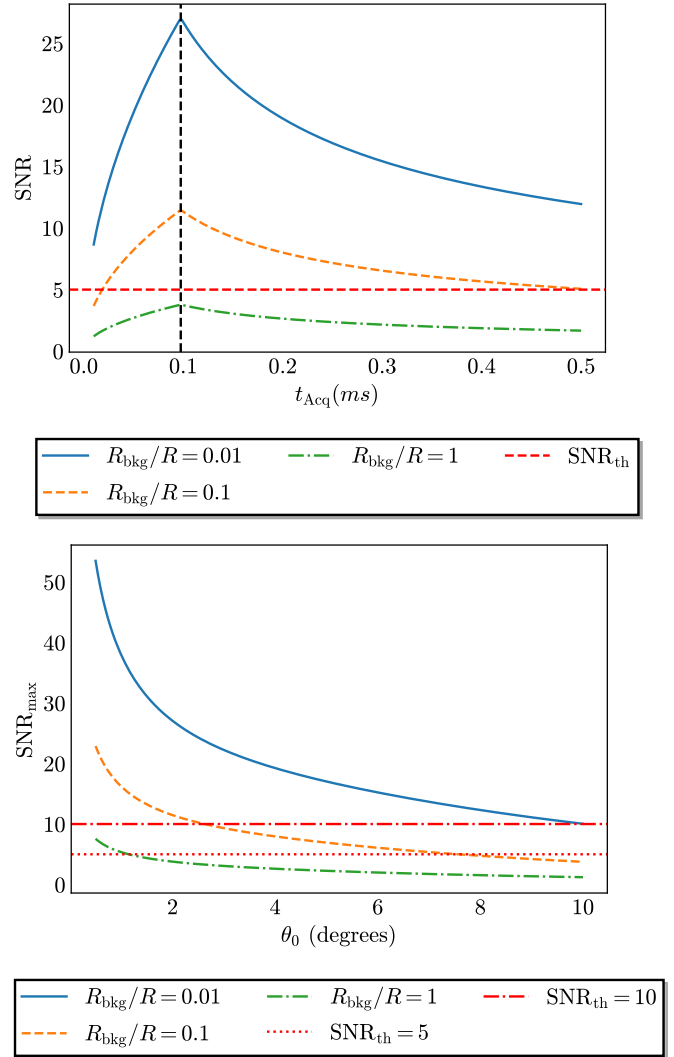
FIG. 5. (top) SNR vs acquisition time for different noise levels (angular separation $\theta_0 = 2°$), clearly maximum SNR is achieved at $t_{\text{Acq}} = t_{\text{Acq}}^{\text{opt}}$ (black dotted line) as expected according to Eq. (22). Also, at higher noise, background levels of the SNR drops below the threshold of $\text{SNR}_{\text{th}} = 5$. (bottom) SNR vs angular separation for different background rates, clearly $\text{SNR} > \text{SNR}_{\text{max}}$ for even very large angular separations when $R_{\text{bkg}} \ll R$. On the other hand when $R_{\text{bkg}} \approx R$, SNR drops below the threshold of $\text{SNR}_{\text{th}} = 5$ for a much smaller angular separation between satellite and ground station.

also satisfied. We show in the subsequent section, using simulation results and also from analytical results obtained in this section, that Eq. (23) is comfortably satisfied for $\text{SNR}_{\text{th}} \approx 5$, whenever the background rate is around two to five times lower than the source rate. For details, see Figs. 5 (bottom) and 8.

IV. SIMULATION METHODS: SYNCHRONIZATION OF A SATELLITE AND A SINGLE GROUND STATION

The simulation of this scenario consists mainly of three parts: (1) simulating the photon generation, (2) simulating the dynamics of the satellite and ground station, and (3) simulating the lossy quantum communication channel between the two parties. We use standard Monte Carlo techniques to

randomly generate photon timestamps at the source, assuming a constant rate R of entangled bits (e-bit) production. We also generate background photons independently at the ground station and satellite at constant rates given by $R_{\mathrm{bkg}}^{\mathrm{gs}}$ and $R_{\mathrm{bkg}}^{\mathrm{sat}}$, respectively (it would be straightforward to add random variability to these rates, mimicking fluctuations in the noise). Furthermore, at every time step we update the positions of the ground station and the satellite to evaluate the link distance and time of travel for the photons that are produced in that time step. The link distance enters as an input into the efficiency η of the free-space communication channel. Further, θ_0, which is the angle between the ground station zenith and the satellite, is calculated from the position vectors. We take into account the various losses by calculating effective efficiency factors both for the uplink (ground station to satellite) and downlink (satellite to ground station) $\eta_{(\mathrm{up})}$ and $\eta_{(\mathrm{dwn})}$, respectively. $\eta_{(\mathrm{up})}$ is the probability that a photon generated out of the SPDC source at the ground station will lead to a double-detection event, i.e., one partner will be detected at A locally and the other at B after traveling through space and the atmosphere. Similarly for $\eta_{(\mathrm{down})}$. For the sake of brevity, the remaining details of the simulation methods are provided in Appendix A.

Once the photons are generated and timestamped, the correlation functions are calculated by counting the number of photons that are generated a time interval τ apart from each other. This is the value of the correlation function $C(\tau)$.

For larger configurations involving multiple satellites and ground stations, and for longer simulation periods (≈ 1 day), it becomes computationally expensive to run the Monte Carlo simulation at the subnanosecond time resolution. It is also not necessary to do so, since all the information about the success and quality of the time synchronization can be evaluated from Eqs. (23) and (25). See Fig. 9 for an illustration.

V. SIMULATION RESULTS

Now we discuss the results obtained from the simulation described in the preceding section. First, in Sec. V A, we look at the simplest scenario of a single ground station located within the orbital plane of the satellite (Fig. 3) in order to quantitatively verify the analytical results obtained in Sec. III. Next, in Sec. V B, we discuss the results for more generic orbits, but restricting ourselves still to a single satellite and ground station pair. We will then introduce the idea of the precision shadow of the satellite, which will help us optimize the satellite configuration and trajectories for the more complicated multiple ground station scenario, which we pursue in Sec. III A. For convenience, the operational parameters used for all simulations are listed in Table I.

A. Single satellite and ground station in the same plane

First, let us study the peak spreading effect due to relative motion. We choose $\theta_0 = 2°$ [which is below $\theta_0^{\mathrm{crit}} \approx 3°$ given by Eq. (28)]. From Eq. (18) and setting $h = 500$ km, we find $t_{\mathrm{Acq}}^{\mathrm{opt}} = 4.8 \times 10^{-5} s$. Figure 6 below shows the results for two different acquisition times, falling in the two regimes $t_{\mathrm{Acq}} = 5 \times 10^{-5}$ s $\approx t_{\mathrm{Acq}}^{\mathrm{opt}}$ and $t_{\mathrm{Acq}} = 10^{-3}$ s $\gg t_{\mathrm{Acq}}^{\mathrm{opt}}$. In the first case, it is clear that sharp peaks can be identified for both the

TABLE I. Various operational parameters for the simulation: notation and choice of values.

Altitude of satellite	$h = 500$ km
Operational wavelength	$\lambda = 810$ nm
Radii of telescopes	$(r_{\mathrm{sat}}, r_{gs}) = (10$ cm$, 60$ cm$)$
Detector efficiencies	$(\kappa_{\mathrm{sat}}, \kappa_{gs}) = (0.5, 0.5)$
Source rate	$R = 10^7$ entangled pairs/s
Simulation time-step (max precision)	$t_{\mathrm{bin}} = 0.5$ ns

correlation functions C_{AB} and C_{BA}. This is quantitatively portrayed by the adjoining plot showing the SNR as a function of τ. Clearly, only one value of τ shows an SNR significantly higher than $\mathrm{SNR}_{th} = 5$. On the other hand, in the latter case it is easy to see the peak broadening, as anticipated in the discussion from Sec. III. The SNR values also highlight the advent of multiple peaks, and the consequent decrease in precision of synchronization.

Next, we investigate the effect of increasing angular separation on the time synchronization. Equation (28) gives an estimate of the maximum critical angle for a given choice of N_{min} at a required level of precision. We choose $t_{\mathrm{Acq}} \approx t_{\mathrm{Acq}}^{\mathrm{opt}}$ from now on, having shown that the protocol can work at optimal precision only under that condition. From Fig. 7, it is evident that, at angles greater than the critical angle, even with no background noise, enough photons cannot be collected within the acquisition time to achieve a clear peak. The SNR values also indicate this effect. Obviously, collecting photons for a longer time will not alleviate the situation since the SNR is just going to fall for $t_{\mathrm{Acq}} > t_{\mathrm{Acq}}^{\mathrm{opt}}$ due to the peak broadening effects just discussed.

Let us now move on to show the effect of background noise on the synchronization outcomes. To study the effect of background noise, we run the simulations at different noise rates. It can be seen from Fig. 8 that the SNR shows significant decrease with increasing R_{bkg} as it grows past the effective rate of detection through the free-space channels, i.e., $R\eta$ [as expected from Eq. (22)]. For simplicity, we choose same background rates at the satellite and at the ground station. In a realistic scenario, this is obviously not true—background rates are much smaller at the ground station. Since the aim here is to just illustrate effect of background photons on the signal-to-noise ratio, we consider this worst-case scenario.

B. Simulation results for a generic satellite orbit

Next, we run the simulation by allowing the ground station to be located in a general location, not necessarily in the plane of satellite's orbit, which is chosen to be a polar orbit. These simulations are run with the understanding that, once the acquisition time is chosen optimally ($t_{\mathrm{Acq}} = t_{\mathrm{Acq}}^{\mathrm{opt}}$), the optimal precision can be achieved. Hence, from here on we use the term precision to mean maximum achievable precision. We stress here that this does not mean that the satellite and ground station trajectories need to be known to perform the QCS successfully. Of course, for any practical application, some information of the trajectories is available. For example, in order to successfully send photons to the satellite, its trajectory must be known at least approximately. Given this knowledge,
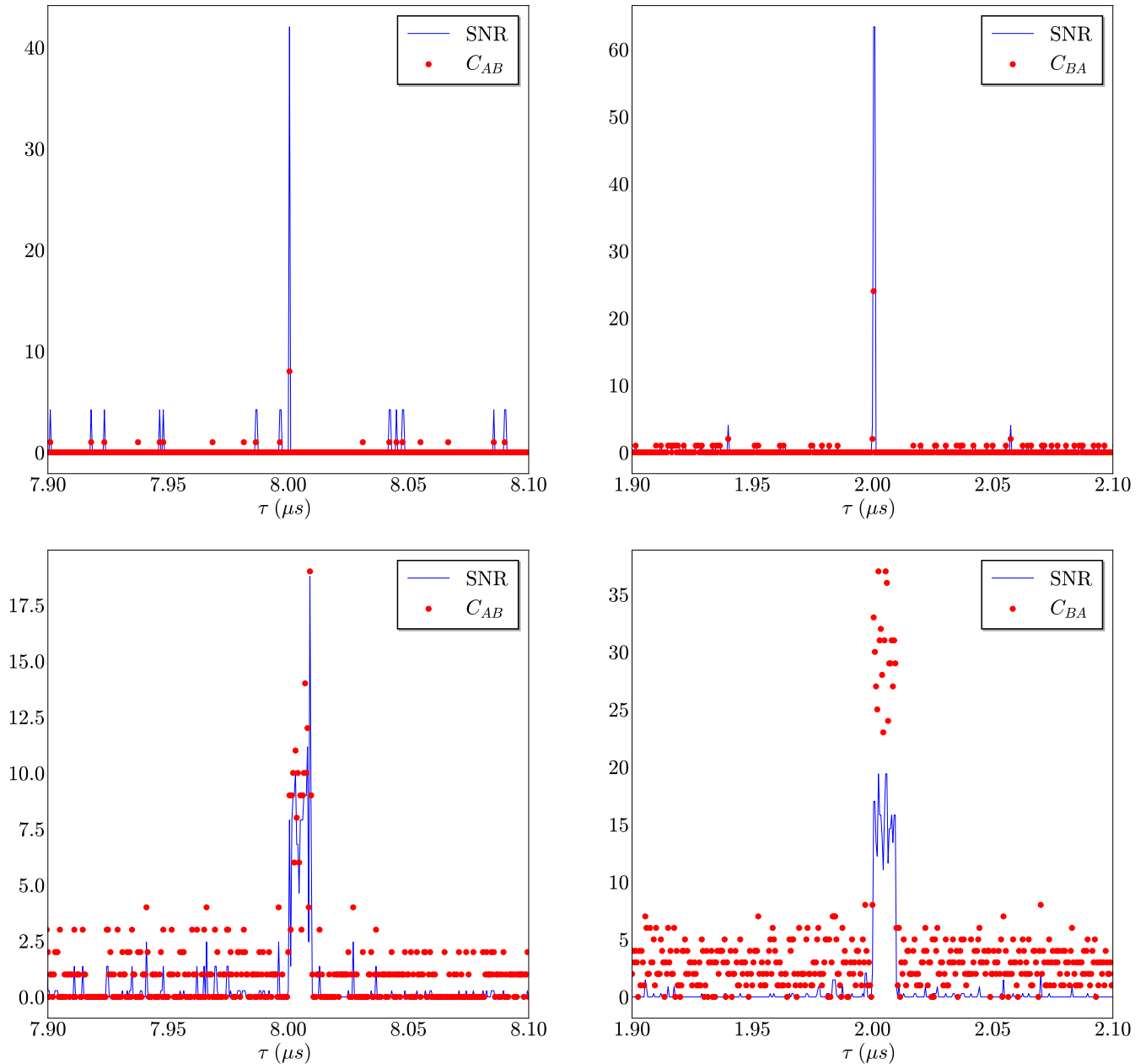
FIG. 6. Uplink (left) and downlink (right) correlation functions (red dots) and respective SNRs (blue continuous line) of all peaks as a function of the time shift τ. For genuine correlations, the expected peaks are at 8 μs for the uplink and 2 μs for the downlink. Top plots represent the $t_{\text{Acq}} \approx t_{\text{Acq}}^{\text{opt}}$ case. Notice that only one peak with substantially high SNR exists; all other peaks are also below the chosen threshold $\text{SNR}_{th} = 5$. For the bottom plots, on the other hand, $t_{\text{Acq}} \gg t_{\text{Acq}}^{\text{opt}}$, and several peaks with high SNR (>5) appear. This introduces uncertainty in the identification of the time offset, and directly reduces the sync precision. Peak-spreading due to motion of the satellite is responsible for the reduced precision. These simulation results support the results in Sec. III that acquisition times of the order of $t_{\text{Acq}}^{\text{opt}}$ must be chosen for the protocol to work at optimal level of precision. The value $R_{\text{bkg}} = 10^6 \text{ s}^{-1}$ has been used for background rate in these simulations. The values used for other parameters are summarized in Table I.

we can either find bounds for the relative velocity, calculate a minimum value for $t_{\text{Acq}}^{\text{opt}}$, and then choose our acquisition time close to this value to run the protocol at near-optimal precision, or we could take an operation view and change the binning of the total acquired data until the SNR crosses the threshold (see Appendix C). The satellite and ground station trajectories need to be known for the purposes of alignment, etc., but the QCS protocol itself does not need either knowledge of the velocity or the position of the satellite or ground

stations. To understand the effect of such a generic orbit on the sync outcomes, let us first look at the two parameters $\mathcal{K}$ and $\eta_{\text{up/dwn}}$ discussed in Sec. IV. The radial velocity of the satellite with respect to the ground station and the link loss are both minimal whenever the trajectory is at a local minimum, i.e., whenever the link distance L or the zenith angle θ_0 are at a local minimum. We call such situations overhead passes of the satellite. For the simulation results shown in Fig. 9, we consider a setting with a polar satellite in orbit at 500 km
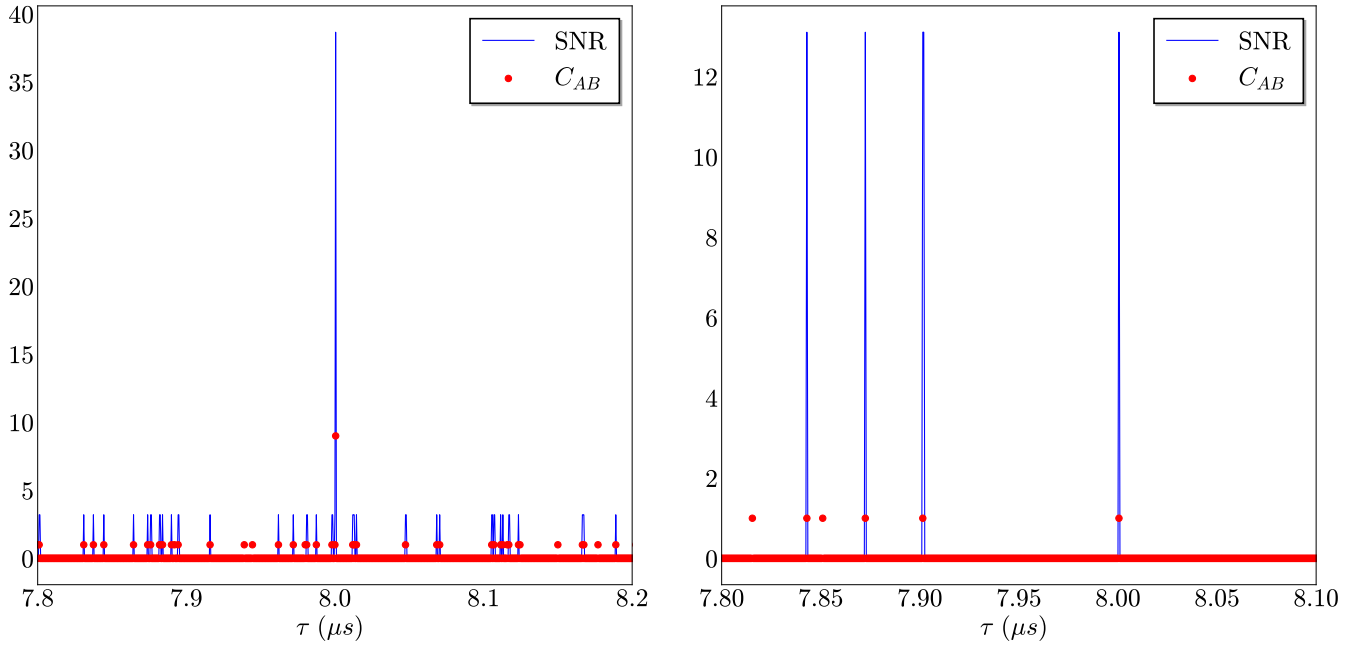
FIG. 7. Uplink correlation function C_{AB} for $\theta_0 = \theta_0^{\text{crit}} \approx 3°$ (left) (the uplink is the weaker link, and determines the success or failure of the protocol). Clearly, there is a unique peak marking the correct time correlations. For comparison, the right panel shows a similar plot for $\theta_0 = 10°$, where multiple peaks are observed. The values for background noise and acquisition time used in these plots are $R_{\text{bkg}} = 10^6$ s^{-1} and $t_{\text{Acq}} = 5 \times 10^{-5}$ s, respectively.

altitude along the prime meridian, and a ground station in New York City (40.7128° N, 74.0060° W). The results clearly show that overhead passes give a high number of double-detection events (a peak in C_{AB} and C_{BA}), and, consequently, a high level of sync precision. For clarity, we define precision as $-\log_{10}(t_{\text{bin}})$, such that a lower value of bin size means a higher precision. Since the precision falls down sharply as the satellite moves past the overhead configuration, we see that an analog of critical angle θ_0^{crit} (see Secs. III and V A) emerges in the generic case as well—the difference being that now it has to be replaced by a solid angle. Such a solid angle can also be described as a shadow the satellite casts over Earth during its motion in its orbit. The shadow describes a region on Earth at a given instant of time, inside which a ground station can synchronize with the satellite at a certain maximum achievable

precision. We now try to estimate the shape and size of such a shadow for different levels of maximum achievable precision.

From the results in Fig. 9, it is clear that the shape and size of the shadow of the satellite not only depends on the link distance L through η but also on the relative radial velocity of the satellite with respect to the ground station $v_{\text{rel}}^{\text{rad}}$ through $\mathcal{K}$. In Fig. 10, we now show the shadow of the satellite as it passes over different parts of Earth. Without lack of generality, we choose the longitude along the prime meridian (since an overall rotation along the Earth's axis for both the ground station and satellite have no effect either on $v_{\text{rel}}^{\text{rad}}$ or on L). Clearly, the shadow changes shape as the satellite moves closer to the poles. This is a combined effect of the change in relative velocity and the fact that that close to the poles, similar azimuthal angle separations lead to shorter distances along the
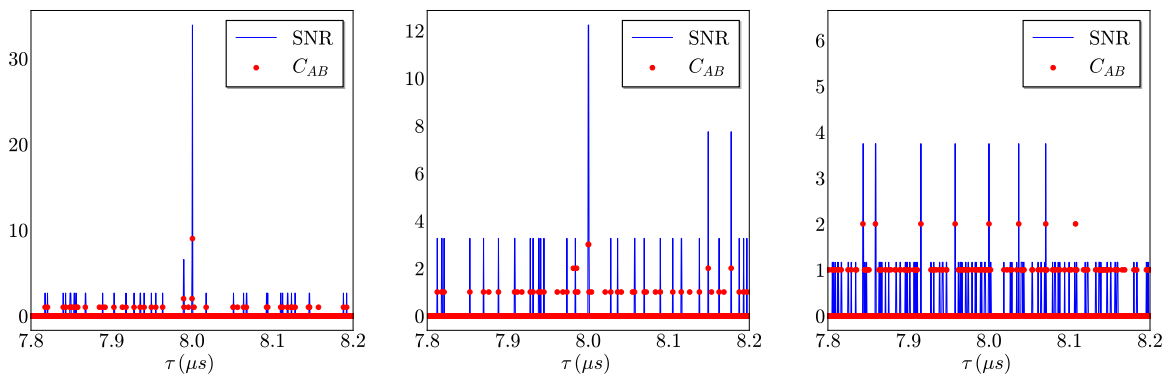
FIG. 8. These plots show the effect of background noise in the correlation functions. Correlation functions and SNR are shown for $\theta_0 = 2°$. This value is below the critical angle given by Eq. (28). The background noise rates are 10^6 photons/s (left), 10^7 photons/s (center), and 10^8 photons/s (right). It is clear that, as the background rate grows past $R\eta = 10^7$/s, the SNR falls below the threshold value SNR$_{th} = 5$, making it less probable to detect a unique peak.
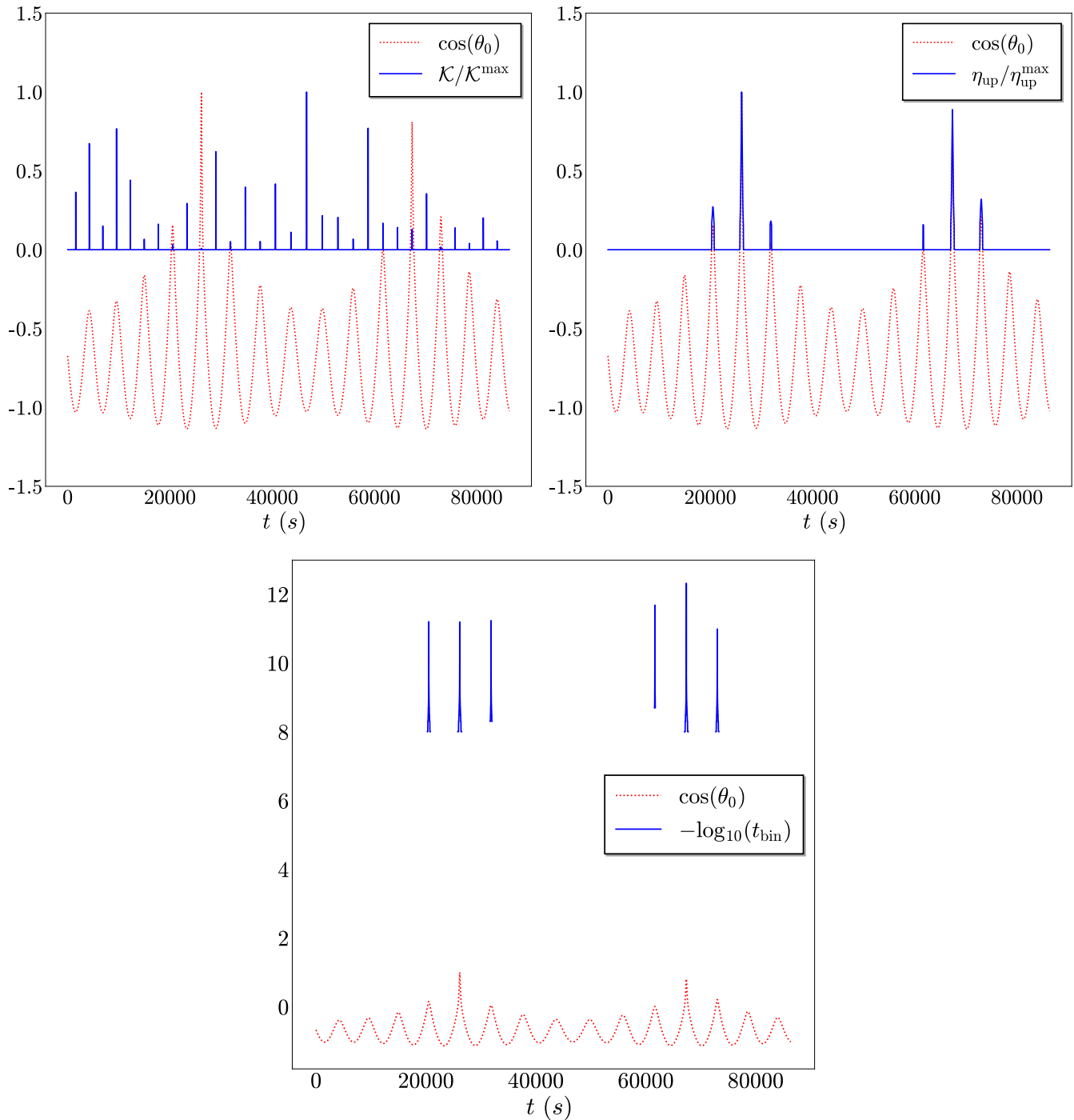
FIG. 9. (top) These plots show values for the two parameters that determine the achievable precision: θ_0 (the angle that the satellite makes with the ground station zenith line) and $\mathcal{K}$ [the geometric factor defined in (18)]. (left) The geometrical factor $\mathcal{K}$ is maximized whenever the derivative of the θ_0 vanishes. The optimal acquisition time $t_{\text{Acq}}^{\text{opt}}$ is proportional to $\mathcal{K}$. (right) The link transmittance η_{up} (recall that the uplink, being the weakest link, determines the limits of precision), as expected, is maximized whenever the link distance L is minimized and hence is maximum for overhead passes. (bottom) The synchronization outcome (blue line) determines the sync precision (it is the negative log of the bin size) and it clearly follows the trends set by the two parameters $\mathcal{K}$ and η_{up} [we choose $N_{\text{min}} = 10$, see Eq. (25)]. A few times during the course of a day, when the link distances are minimized (overhead passes), the precision levels surpass the nanosecond level and even approach the picosecond level. These sync outcomes are currently not achievable by classical techniques for space-based communication like the GPS. The discontinuity in the precision curve (also the transmittance curve) is a consequence of the horizon condition [Eq. (A8)].
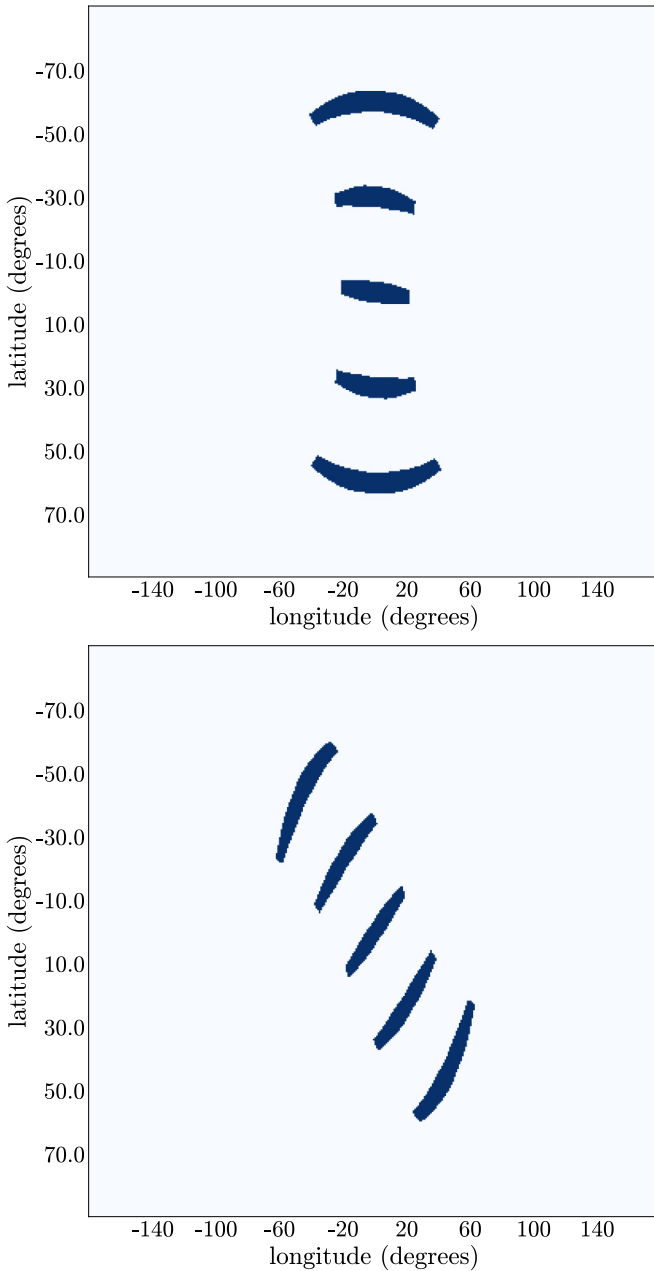
FIG. 10. "Precision shadow" of a satellite as it passes over different parts of Earth. A shadow refers to a region within which a certain sync precision can be achieved. Here, within the black shadow a precision of at least 1 ns can be achieved. During real time dynamics the shadow will be a continuous track along the orbit of the satellite. Snippets in time are shown here to illustrate the changing shape and angular size of the shadow as the satellite moves. (top) Polar orbit along the prime meridian. (bottom) Tilted polar orbit, rotated by $30°$ compared with the case on the left. In both cases the extent of the shadow close to the equator is $\approx 50°$ perpendicular to the satellite trajectory and $\approx 3°$ along the trajectory.

surface of Earth compared with near the equator. The latter is the more significant reason, thus this morphing of the shadow shape should be considered primarily a map projection effect and not a physical effect. The shadow is closest to an ellipse near the equator, the minor axis being along the direction of

satellite motion and the major axis perpendicular to it. This is expected since the satellite velocity is the major contributor to $v_{\mathrm{rel}}^{\mathrm{rad}}$, and a higher relative velocity means a smaller t_{Acq}. In other words, the critical angle θ_0^{crit} along the direction of satellite motion is the smallest and is the largest perpendicular to the direction of satellite motion. In contrast, if the precision were to just depend on the total number of counts received with no restriction on the acquisition time, the shadow would have been a circle, i.e., same level of precision would have been achieved for points equidistant from the satellite since the loss function is monotonically decreasing with increasing L. For tilted orbits, the trends remain similar. The shadow still has its minor axis along the orbit of the satellite. We get a tilted ellipse close to the equator which becomes more and more morphed as one moves closer to the poles. These trends are also shown in Fig. 10. In both cases the extent of the shadow close to the equator is $\approx 50°$ perpendicular to the satellite trajectory and $\approx 3°$ along the trajectory. Another important factor in determining the extent of the shadow is the horizon condition. This sets a cutoff for the shadow size, irrespective of the possible acquisition time and the link loss. In Fig. 11, we show the effect of the horizon condition in determining the size of the satellite shadow. It is also interesting to look at how the extent of the shadow reduces as one makes the sync requirements more stringent. In Fig. 11 (bottom) we show the regions within the shadow where different sync capabilities can be achieved. As expected, the closer one is to the center of the shadow, i.e., the closer one is to the overhead case, the higher the achievable sync precision.

In summary, in this section we have presented the main results of our numerical analysis. The main output of our simulations are the precision shadows of a satellite, shown in Fig. 10. Through these shadows we concretely determine the region on Earth within which two ground stations can be synchronized by means of a satellite at a minimum required level of precision. This information is crucial to determine the size and quality of a QCS network [11]. Our numerical code can be used to obtain these shadows and their time evolution for satellites in arbitrary orbits and assist in the design of optimal satellite constellations for time distribution.

VI. SYNCHRONIZING MULTIPLE GROUND STATIONS

Let us now use the results of the shadow picture to achieve a practical sync requirement. Consider four major cities on geographical corners of the continental United States, namely: New York, Atlanta, Los Angeles, and Seattle. Let us now ask the following question: "What are the best synchronization outcomes that can be achieved for these four cities using a single satellite in a LEO?" We believe this question to be pertinent from two points of view: (1) It describes a proof of principle realization of the proposed QCS protocol using intermediary satellites and therefore paves a way for more ambitious implementations, like augmenting a global quantum internet, building a quantum GPS, etc. And (2) such small-medium scale realizations themselves may have practical benefits, such as time distribution for sensitive scientific experiments, high-precision secure time transfer for civil and defense uses, etc.
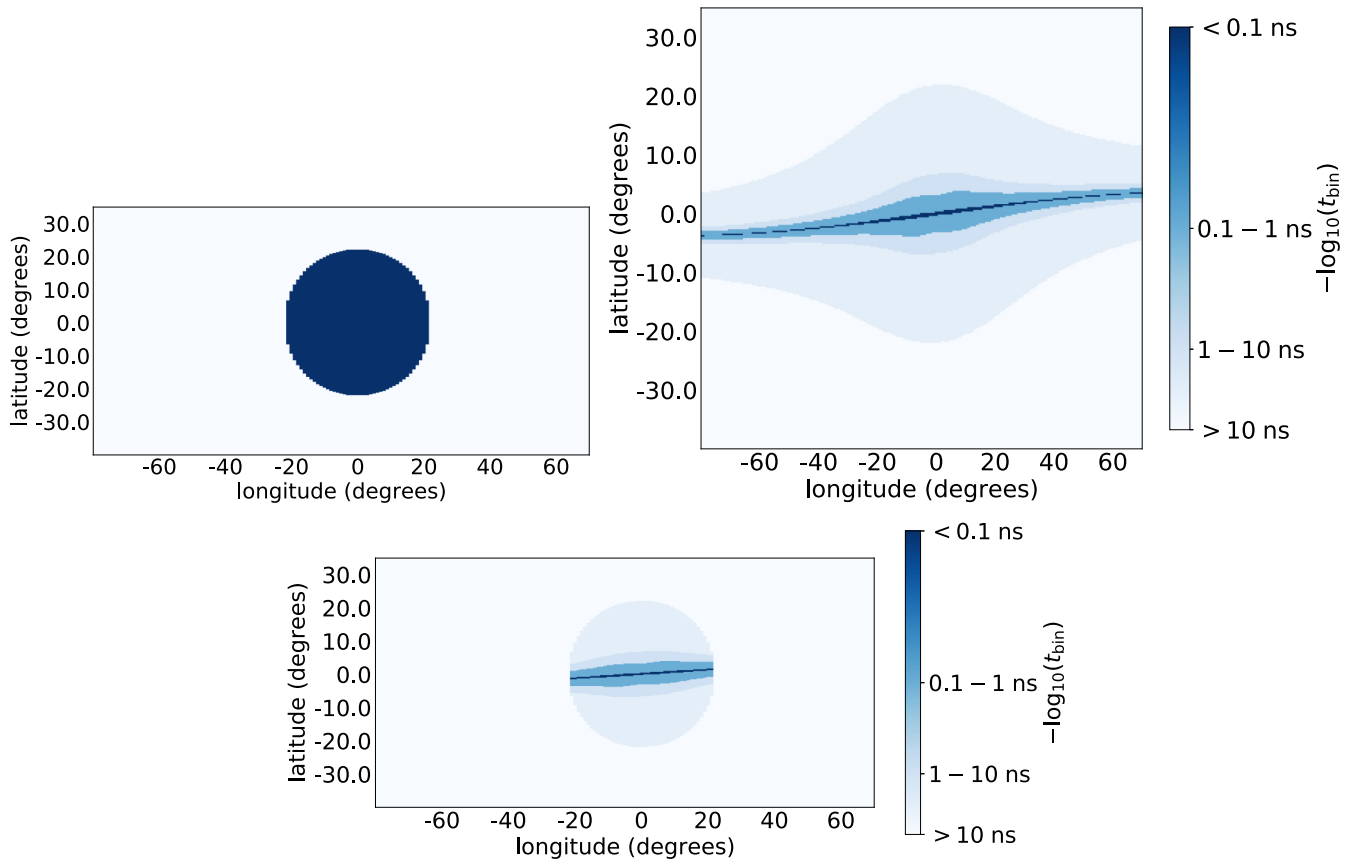
FIG. 11. (top left) Region of visibility on Earth of a satellite, which in this example we have placed directly above the intersection of the prime meridian and the equator. (top right) Regions where a ground station can sync with the satellite at different precisions indicated by different colors. Innermost region can sync at the highest precision since the relative radial velocity is the lowest around overhead pass. This plot does not include the condition of visibility. (bottom) The precision shadow of the satellite, obtained by superposition the top two figures. This precision shadow is the main output of our calculation and contains information about the size and quality of the network.

Let us first trace out the shadow of the satellite when it is above the center of the ground station configuration mentioned above. This tells us that all four cities cannot be synced simultaneously since the shadow is not wide enough (latitude-wise) to contain all four cities at any given instant (see Fig. 12). We verify this by looking at the uplink photon counts received simultaneously by each pair of cities. A sync at a given precision is considered successful if both the cities see the satellite (satellite is above the horizon for both) and more than a cutoff number of correctly correlated photons are received by each of them in accordance with Eq. (25). The sync precision is given by the minimum of the two sync precision values obtained, namely, precision of sync between ground station 1 (GS1) and the satellite and precision of sync between GS2 and the satellite. We find, as expected, that only the New York–Atlanta and Atlanta–Los Angeles pairs can be synced at a precision higher than or equal to 1 ns. The latitude difference between the other pair of cities is more than the width of the shadow.

Therefore, now we must relax the sync requirements. If we allow even modestly stable clocks on the satellites (standard rubidium clocks can hold time up to 1 ns precision for around

10 mins) then we can relax the condition of simultaneous connectivity between the three parties viz. the satellite, and the two ground stations. We can instead define a holdover time τ within which, if the satellite connects to both cities, the two cities are considered synchronized. Larger holdover times lead larger sync coverage areas because they allow the satellite to reach stations that are located further away. But of course such an improvement comes at a cost. Since, earlier we were only considering simultaneous connection between GS1, GS2 and the satellite, the precision of the protocol was limited only by the sync precision, assuming that the satellite and ground station clocks can timestamp with much higher precision compared with the sync precision. If we allow for a holdover time, this no longer remains true. The precision of the protocol will be determined not only by the sync precision but also by the precision of the least stable clock. It is reasonable to assume that the ground station clocks will be much more stable than the smaller and lighter clocks onboard a satellite. Therefore, if at a given instant t there is connection between the satellite and ground station 1, then we look for the best precision connection between the satellite and ground station 2 within the interval $(t - \tau/2, t + \tau/2)$. The
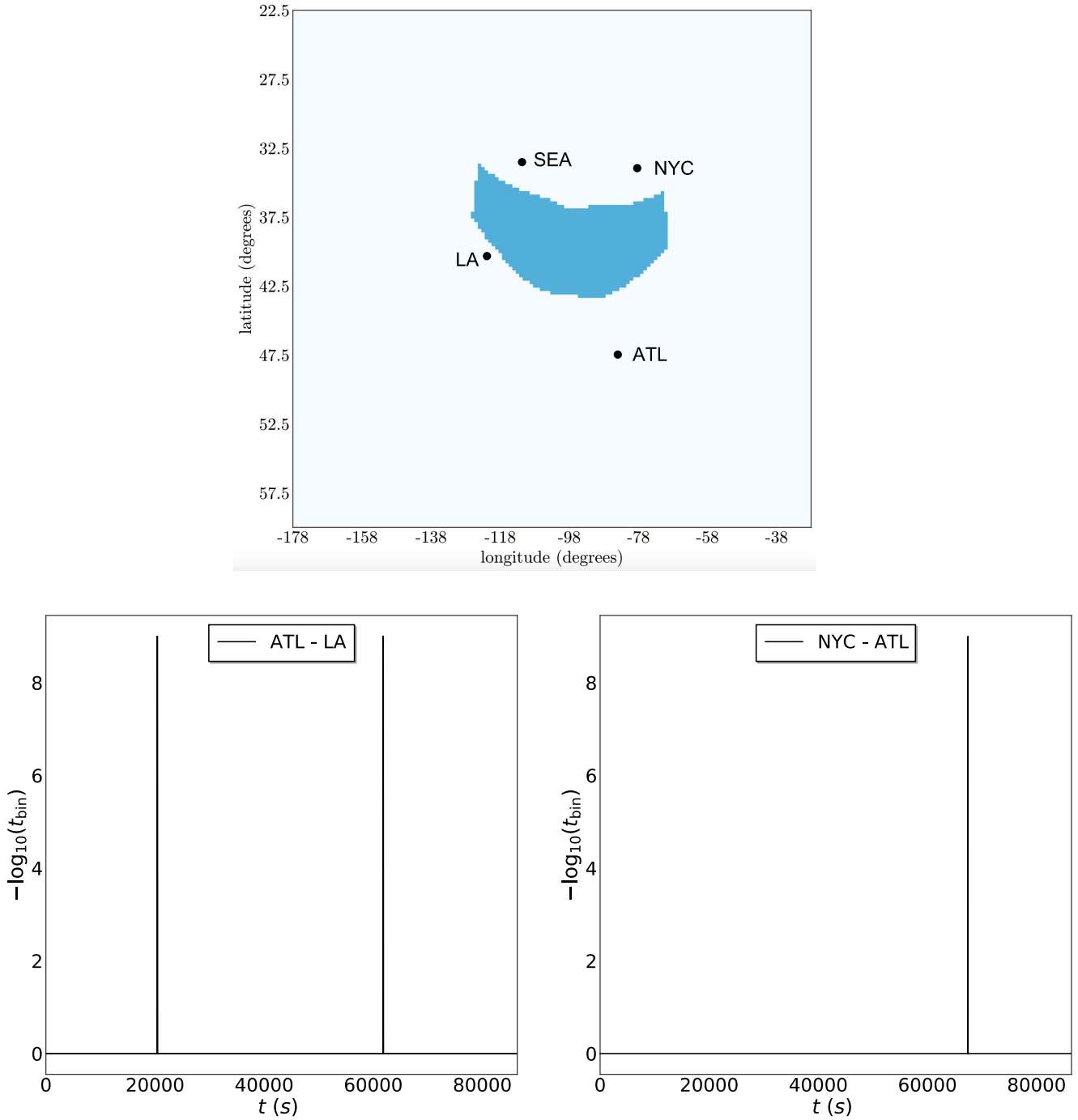
FIG. 12. (top) Satellite shadow when it is just above the center of the ground station configuration NYC-ATL-LA-SEA. All city pairs do not fall within the shadow and hence cannot be simultaneously synchronized. The only two pairs whose latitude difference is less than the width of the shadow are ATL-SEA (bottom left) and NYC-ATL (bottom right). Subnanosecond precision can be achieved at least once a day in both these cases.

precision of connection at time t between the two ground stations defined as

$$- \log_{10} \left(t_{\text{bin}}^{GS1-GS2} \right)(t)$$

is given by the following expression:

$$\max_{t' \in (t-\tau/2, t+\tau/2)} \left(\min \left[- \log_{10} \left(t_{\text{bin}}^{GS1-SAT} \right)(t), - \log_{10} \left(t_{\text{bin}}^{GS2-SAT} \right)(t'), - \log_{10} \left(t_{\text{bin}}^{\text{sat}} \right)(t') \right] \right). \tag{29}$$
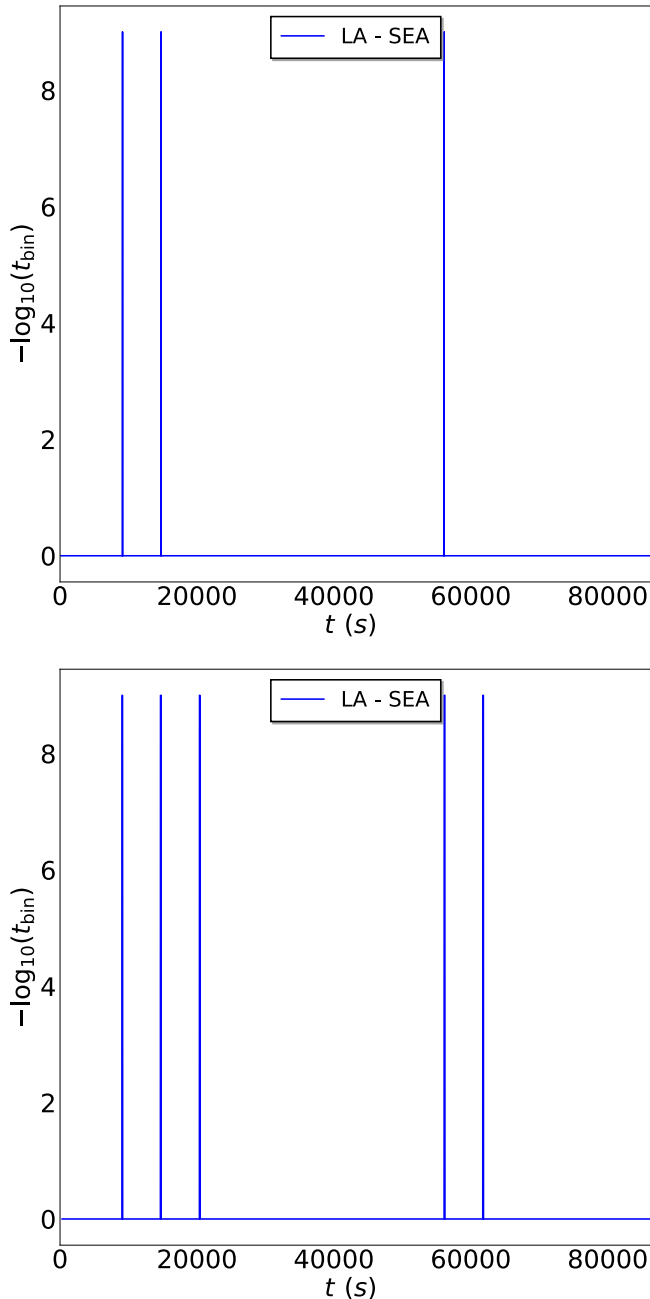
FIG. 13. Improvement in sync outcomes between Los Angeles and Seattle, both in terms of precision and the number of connections every day, as the holdover time τ is increased from $\tau = 240s$ to $\tau = 600s$.

In general, the precision of a clock and hence $-\log_{10}(t_{\text{bin}}^{\text{sat}})(t')$ is a complicated function of time. In fact the Allan deviation curve which is the standard measure of a clock's stability, is often obtained empirically. Here, for our simulations we take a simplistic, worst-case-scenario approach:

$$-\log_{10}\left(t_{\text{bin}}^{\text{sat}}\right)(t') = \begin{cases} C, & t - \tau/2 < t' < t + \tau/2 \\ 0, & \text{otherwise,} \end{cases} \quad (30)$$

where C is a constant level of precision. Figure 13 shows the improvement in sync outcomes as the holdover time is increased for SEA-LA. For $\tau = 0$ there was no connection at

the 1 ns precision, and as τ is increases, we see more frequent connections.

Figure 14 shows that, for $\tau = 600$ s (10 min), six city pairs in the configuration can be synced at the 1 ns precision [$C = 1$ ns in Eq. (30)] more than once a day, in contrast with the $\tau = 0$ case where only 2 city pairs could be synced [Fig. 12(bottom)]. Even though nanosecond level precision can be achieved using a single LEO satellite for the continental US, the connectivity is sparse, with long disconnected intervals between sync events. This situation can be easily alleviated by using a larger constellation of satellites (both adding satellites to same orbit and using multiple orbits). Optimization of satellite resources both in terms of constellation design and onboard system parameters is a complex problem. For a more concrete analysis of figures of merit such connection fractions of the day and longest disconnected intervals (at required levels of precision) which quantify the connectivity of various QCS network designs and system parameters, we refer the reader to a previous work [1].

VII. CONCLUSIONS AND FUTURE WORK

In this paper, we have assessed the feasibility of a quantum clock synchronization network using satellites. We have developed a numerical code to simulate the real-time implementation of a QCS protocol, including the effects of relative velocities, photon losses, background noise and detector jitter. Although results presented here are based on some simplifying assumptions, such as constant source and background rates and circular polar orbits, ignoring effects of cloud cover and other weather conditions, etc., the general framework of our code is receptive to loosening these constraints. Our code is versatile and can be adapted to any given network of ground stations and satellites. Our results are generic in this sense and crucially the trends for network quality and size shown here are supportive of the usefulness of a quantum timing network based on QCS, albeit requiring a more systems and engineering level feasibility study. Furthermore, our code can be also used to analyze quantitatively other entanglement distribution based protocols such as device-independent QKD, quantum communication networks, etc.

Our detailed analysis has shown that it is possible to provide subnanosecond to picosecond level synchronization outcomes for a network spread across the continental US. This is a network size of around 4000 km. It is important to mention that no classical or quantum techniques presently available can provide such precision levels over distances which are this long. We thus propose the QCS network with space-terrestrial optical communication links as the method of choice for high precision, long-range time distribution. Since the QCS protocol is yet to be tested between moving clocks, our analytical and simulation results build the ground for future implementations. For future work we consider the establishment of a master clock in the sky, by interlinking satellites through QCS. By establishing continuous network coverage on global scales, this provides an opportunity to create a high-precision quantum-secure infrastructure for long-distance positioning, navigation, and timing services.
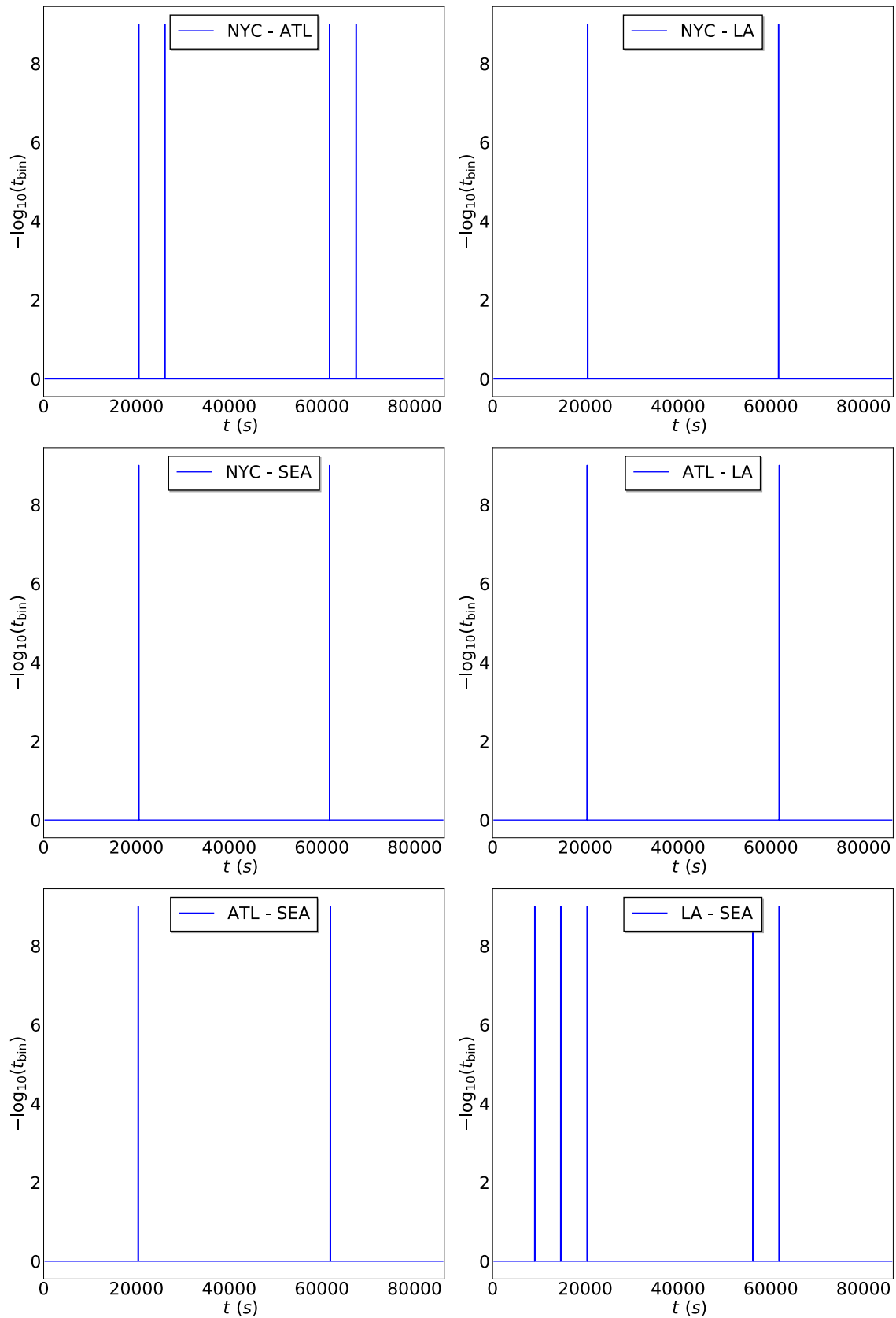
FIG. 14. Sync outcomes between all six city pairs for a holdover time $\tau = 600s$ (10 min). Nanosecond precision can now be achieved in all cases in contrast with the situation with $\tau = 0$ where only two city pairs could achieve the required precision levels.

APPENDIX A: DETAILS OF THE SIMULATION MODEL

The pure-loss model for the free-space quantum communication channel is quantified by a single transmissivity parameter η. η has three contributions:

i. Free-space transmittance: This includes effects of beam broadening and finite apertures of the transmitting and receiving telescopes. The free-space transmittance follows an inverse square falloff law with the link distance and is given by

$$\eta_{\text{fs}}(L) = 1 - \exp\left(-\frac{2R^2}{[w(L)]^2}\right), \tag{A1}$$

where R is the receiving telescope's radius and $w(L)$ is the beam waist after traversing the link distance L. The latter is given by

$$w(L) := w_0\sqrt{1 + \left(\frac{L}{L_{\text{R}}}\right)^2}, \tag{A2}$$

and the Rayleigh range $L_{\text{R}} := \pi w_0^2 \lambda^{-1}$. λ is the source wavelength, and w_0 is the initial beam-waist radius. $w_0 = 0.8r$, where r is the transmitting telescope's radius and we use a 80% fill fraction. The above relation holds under the approximation of the beam as a zeroth-order Gaussian spatial mode.

ii. Atmospheric transmittance: Here we assume the atmosphere to be a homogeneous absorptive medium following the Beer-Lambert law (transmittance falls exponentially with increasing distance that is traveled through the medium). Thus, the atmospheric transmittance is given by

$$\eta_{\text{atm}}(L, h) = \begin{cases} \left(\eta_{\text{atm}}^{\text{zen}}\right)^{\sec\zeta}, & \text{if } -\frac{\pi}{2} < \zeta < \frac{\pi}{2} \\ 0, & \text{if } |\zeta| \geqslant \frac{\pi}{2}, \end{cases} \tag{A3}$$

where η_{atm}^{zen} is the atmospheric transmittance at zenith ($\zeta = 0$) and the zenith angle ζ for circular orbits is given by

$$\cos\zeta = \frac{h}{L} - \frac{1}{2}\frac{L^2 - h^2}{R_E L}, \tag{A4}$$

where R_E is the radius of Earth.

iii. Detector inefficiencies: κ_{sat} and κ_{grd} are efficiencies of the detectors at the satellite and ground station, respectively.

Thus, the total efficiency of the channel (uplink or downlink) is given by $\eta = \eta_{\text{atm}}\eta_{\text{fs}}\kappa_{\text{sat}}\kappa_{\text{grd}}$.

Given the above loss model we model the satellite-ground quantum communication channel as follows: For concreteness, let us focus on a downlink channel. The following will hold similarly for an uplink channel. We assume clear skies and approximate the downlink channel as only lossy (background noise is accounted for at the detectors). That is, photons are either transmitted through the channel or lost in transmission. The dominant sources of loss are (1) beam spreading (free-space diffraction loss), (2) atmospheric absorption or scattering, and (3) nonideal photodetectors on the satellite and on the ground. We characterize these loss mechanisms by their transmittance values, which is the fraction of the received optical power to the transmitted power (which is also equal to the probability to transmit or detect a single photon). Let these transmittance values be, respectively,

$$\eta_{fs}^{(\text{dwn})}(L), \ \eta_{atm}^{(\text{dwn})}(L), \ \kappa_{\text{sat}}, \ \kappa_{gs},$$

where the superscripts refer to the downlink, fs refers to free-space diffraction loss, atm to atmospheric loss, L is the link distance (physical distance) between satellite and receiver (which in turn depends on the satellite altitude h, position of the satellite in its orbit, and position of the ground station on Earth's surface), κ denotes nonideal detection efficiencies for the onboard satellite detector array (*sat*) as well as the detector array at the ground station (gs), and all transmittance values are less than or equal to 1. Simple analytic formulas are used to estimate the free-space and atmospheric transmittance values in accordance with Ref. [6]. See Eqs. (A1)–(A4). Therefore, the overall efficiencies are given as

$$\eta_{(\text{dwn})} = \eta_{fs}^{(\text{dwn})}\eta_{atm}^{(\text{dwn})}\kappa_{\text{sat}}\kappa_{gs}, \tag{A5}$$

$$\eta_{(\text{up})} = \eta_{fs}^{(\text{up})}\eta_{atm}^{(\text{up})}\kappa_{\text{sat}}\kappa_{gs}. \tag{A6}$$

Finally, following standard Monte Carlo techniques, our code works by registering a joint detection event (two photons from the same pair detected at A and B) every time two random numbers r, r' independently generated from a uniform distributions $\in [0, 1]$ satisfy the following conditions in the same time step:

$$r < Rt_{\text{bin}}, \tag{A7}$$

$$r' < \eta. \tag{A8}$$

For the noise photons to be detected at A or B, a condition analogous to Eq. (A7), $r'' < R_{\text{bkg}}t_{\text{bin}}$, is used, where r'' is also a random number chosen independently from a uniform distribution $\in [0, 1]$. Furthermore, a condition that the satellite be above the ground station's horizon is already imposed via Eq. (A3).

Once the photons are generated and timestamped, the correlation functions are calculated by counting the number of photons that are generated a time interval τ apart from each other. This is the value of the correlation Function $C(\tau)$.

For larger configurations involving multiple satellites and ground stations, and for longer simulation periods ($\approx$1 day), it becomes computationally expensive to run the Monte Carlo simulation at the subnanosecond time resolution. It is also not necessary to do so, since all the information about the success and quality of the time synchronization can be evaluated from Eqs. (23) and (25). See Fig. 9 for an illustration.

APPENDIX B: SIGNAL-TO-NOISE RATIO OF THE CORRELATION FUNCTIONS

The sharpness of the correlation function peak can be quantified through the signal-to-noise ratio (SNR). This depends on (i) the height of the peak from correctly correlated photons [photons whose timestamps are related by Eqs. (1) and (2)], and (ii) the average noise level (spurious peaks) of the correlation function.

Let us look at the threshold due to noise. The peak due to correct correlations should breach this threshold to be detectable. This threshold arises from the following two sources:

i. Spurious correlations among source photons. Every source photon detected by A has some time correlation

with every photon detected at B, but the correct time correlation given by Eq. (1) or (2) with only one photon, which is its entangled pair partner. All the other correlations form a uniformly distributed threshold level. Total number of correlations (spurious + correct), $N_{\text{total}} <$ is given by the area under the C curve. A simple substitution of Eqs. (3) and (4) into (5) and then integrating with respect to time gives:

$$N_{\text{total}} = \int_0^{t_{\text{Acq}}} C \, dt = R^2 \eta t_{\text{Acq}}^2. \quad \text{(B1)}$$

The number of correlated photons detected in time t_{Acq}, N_{corr}, is given by

$$N_{\text{corr}} = R \eta t_{\text{Acq}}. \quad \text{(B2)}$$

Therefore, the number of spurious correlations N_{spur} is given by

$$N_{\text{spur}} = N_{\text{total}} - N_{\text{corr}} = R \eta t_{\text{Acq}}(R t_{\text{Acq}} - 1) \approx R^2 \eta t_{\text{Acq}}^2. \quad \text{(B3)}$$

The last approximation holds since the total number of photons generated within the acquisition time $R t_{\text{Acq}} \gg 1$, for reasonably high source rates ($\approx 10^6$–10^7 ebits/s). From Eq. (B3) we get the mean height of such spurious correlations to be

$$\bar{C}_{\text{spur}} = \frac{N_{\text{spur}}}{N_{\text{bins}}} = \frac{R^2 \eta t_{\text{Acq}}^2}{t_{\text{Acq}}/t_{\text{bin}}} = R^2 \eta t_{\text{Acq}} t_{\text{bin}}. \quad \text{(B4)}$$

ii. Noise from background. Thermal photons, photons from the sun, radiation in space, dark counts, etc., might lead to further photon timestamps which are not correctly correlated. They appear independently at A and B and hence they also form a uniformly distributed threshold in the correlation function C_{AB}. The average number of correlations due to background photons, again following an argument similar to above, is given by

$$\bar{C}_{\text{bkg}} = R R_{\text{bkg}} t_{\text{Acq}} t_{\text{bin}}, \quad \text{(B5)}$$

where $R_{\text{bkg}} = R_{\text{bkg}}^{\text{sat}}$ and $R_{\text{bkg}} = R_{\text{bkg}}^{\text{gs}}$ for C_{AB} and C_{BA}, respectively, are the background photon rates at the ground station and the satellite. Furthermore, if the dark count rate for the detectors is given by R_{dc}, then an analogous additional term is added to the average noise level, given by

$$\bar{C}_{\text{dc}} = R_{\text{dc}}(R \eta + R_{\text{bkg}} + R_{\text{dc}}) t_{\text{Acq}} t_{\text{bin}}. \quad \text{(B6)}$$

Here we assume that $R \gg R_{\text{dc}}$. Also for (LEO) satellite-based implementations, since $\eta \approx 0.01$, we have assumed background rates $R_{\text{bkg}} \gg R \eta$ and $R_{\text{bkg}} \gg R_{\text{dc}}$. Therefore, $C_{\text{dc}} \ll C_{\text{bkg}}$, and its effect on the SNR has been ignored in this work. Nonetheless, the framework in general allows for its inclusion by introducing a term like Eq. (B6).

The total average height of the noise is, therefore, given by

$$\bar{C}_{\text{noise}} = \bar{C}_{\text{spur}} + \bar{C}_{\text{bkg}}. \quad \text{(B7)}$$

Now, we can evaluate the SNR. The SNR is defined as the ratio of the height of the correlation function peak above the threshold level and the standard deviation of the noise (background + spurious correlations). The noise follows a standard Poisson distribution, and hence the mean is equal to the variance.

The SNR is distinct in the following two time regimes:

i. $t_{\text{Acq}} \leqslant t_{\text{Acq}}^{\text{opt}}$

$$\text{SNR} = \frac{C(\tau_{\text{max}}) - \bar{C}_{\text{noise}}}{\sqrt{\bar{C}_{\text{noise}}}}. \quad \text{(B8)}$$

using the Equations (B3)–(B6) we get

$$\text{SNR} = \sqrt{\frac{\eta}{t_{\text{bin}}(1 + R_{\text{bkg}}/R\eta)}} (1 - R t_{\text{bin}}) \sqrt{t_{\text{Acq}}}. \quad \text{(B9)}$$

In this regime, there exists only one peak due to correctly correlated photons and the SNR increases with t_{Acq}. Also, $R t_{\text{bin}} < 1$ for the SNR to make sense. This translates into the fact that each photon should have a unique timestamp within the precision of the clocks. In fact, for reasonable choices of R and t_{bin} (e.g., see Table I), $R t_{\text{bin}} \ll 1$. Therefore,

$$\text{SNR} \approx \sqrt{\frac{\eta}{t_{\text{bin}}(1 + R_{\text{bkg}}/R\eta)}} \sqrt{t_{\text{Acq}}}. \quad \text{(B10)}$$

ii. $t_{\text{Acq}} > t_{\text{Acq}}^{\text{opt}}$.

Multiple peaks now start appearing. Spurious correlations will now also add to the older peaks, hence not all peaks are of equal height, the average height can be approximated as

$$C(\bar{\tau}_{\text{peak}}) \approx R \eta t_{\text{Acq}}^{\text{opt}} + R R_{\text{bkg}} t_{\text{Acq}} t_{\text{bin}} + R^2 \eta t_{\text{Acq}} t_{\text{bin}}. \quad \text{(B11)}$$

Therefore, using Eq. (B8), the SNR in this case is given by

$$\text{SNR} \approx \mathcal{K} \sqrt{\frac{\eta t_{\text{bin}}}{\sqrt{(1 + R_{\text{bkg}}/R\eta)}}} \frac{1}{\sqrt{t_{\text{Acq}}}}. \quad \text{(B12)}$$

Therefore, for $t_{\text{Acq}} > t_{\text{Acq}}^{\text{opt}}$, the SNR decreases as $(t_{\text{Acq}})^{-1/2}$.

This analysis clearly indicates that the SNR is maximum for $t_{\text{Acq}} = t_{\text{Acq}}^{\text{opt}}$ and hence,

$$\text{SNR}_{\text{max}} \approx \sqrt{\frac{\eta \mathcal{K}}{(1 + R_{\text{bkg}}/R\eta)}}. \quad \text{(B13)}$$

APPENDIX C: OPERATIONAL POINT OF VIEW: HOW TO GET THE BEST AVAILABLE LEVEL OF PRECISION?

The limiting value of t_{bin} found via Eq. (25), in conjunction with Eq. (B13) is calculated using the relative radial velocity $v_{\text{rel}}^{\text{rad}}$ of the satellites with respect to the ground station. From an operational point of view, the QCS protocol does not require the knowledge of $v_{\text{rad}}^{\text{rad}}$ and a high degree of precision can be achieved without using any estimate of relative velocity.[2] When a satellite is visible from a certain ground station, the satellite holdover time τ may allow several rounds of the QCS protocol to be conducted (where the true unknown

---

[2]This does not eliminate the need for tracking of the satellite for the purposes of alignment etc., the algorithm to find the offset does not need the knowledge of the ground station and satellite positions or velocities.
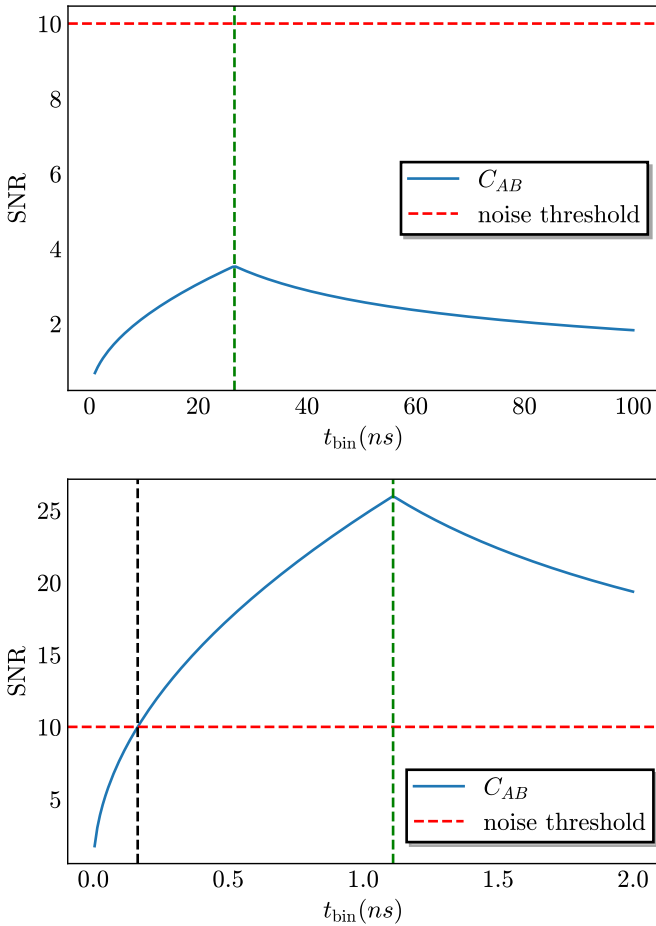
FIG. 15. Here we show that precision obtained at the threshold SNR can be substantially higher than what is achievable if we work the max SNR setting. Source rate and background rates are set at 10^7 ebits/s and 10^4 photons/s, respectively. Loss and relative radial velocity numbers are representative of a 500 km polar orbit passing over New York City. (top) A very oblique pass of the satellite over the ground station leads to a high loss (35 dB) and high relative velocity (4 km/s) setting. In such cases, the max SNR is less than the threshold SNR, and, hence, even though we have visibility, the protocol fails at all levels of precision. (bottom) For a slightly less oblique pass (25 dB loss and 1 km/s relative velocity), working in the threshold SNR regime can provide a precision 10 times higher than what can be achieved by working at the maximum SNR.

FIG. 16. Effect of detector jitter on the precision shadows for 1 ns precision—red (intermediate shaded region in top figure and outermost in bottom figure) shadow represents the jitterless case, green shadow (innermost shaded region in top figure and intermediate region in bottom) represents the shadow for 300 ps of jitter if the precision is determined using Eq. (D1) (N_{min} condition), whereas the blue shadow (outermost shaded region in top and innermost in the bottom) represents the shadow if Eq. (D3) (SNR condition) determines the precision. (top) Precision shadow for low background rate $R_{bkg}/R = 10^{-2}$, Eq. (D1) dominates over Eq. (D3) in determining the maximum achievable precision. (bottom) Precision shadow for high background rate $R_{bkg}/R = 0.5$, Eq. (D3), i.e., the SNR condition dominates over Eq. (D1) in determining the maximum achievable precision.

offset remains the same up to a maximum required precision). Once the timestamp data are collected, the cross-correlation functions must be calculated, which requires choosing a bin size (working precision of the protocol t_{bin}). We must at the same time also choose an acquisition time window t_{Acq}, since, over the total visibility or holdover period, large amounts of data are collected which if used in their entirety to plot the correlation functions will lead to substantial peak spreading and loss of SNR. Therefore, the data must be divided into smaller acquisition windows. Let us begin with the smallest possible t_{bin} (could be the timestamp resolution) and the largest possible t_{Acq} (full timestamp data set available). We would then be working in the regime where the SNR follows Eq. (B12) and is proportional to $\sqrt{t_{bin}/t_{Acq}}$. The SNR thus depends on the ratio t_{bin}/t_{Acq}, as t_{bin} is increased and t_{Acq}

is decreased this ratio increases, increasing the SNR up to the point that it reaches SNR_{max}. We know that $t_{bin}/t_{Acq} = \kappa$ for this optimal setting [see Eq. (B13)]. In practice, though, the following approach could be taken: t_{bin} is increased and t_{Acq} decreased up to the point $SNR = SNR_{th}$, at the same time ensuring $R\eta t_{Acq} \geqslant N_{min}$. The latter condition is needed to ensure the success of protocol with high probability. For instance, even if the $SNR > SNR_{th}$, $R\eta t_{Acq} < 1$ would mean that for some acquisition windows no ebit will be shared between the ground station and satellite, thus the offset would not be obtainable from that round of the protocol. The larger the value of N_{min}, the larger the probability that each run of the protocol gets some shared ebits. This gives an operational meaning to N_{min}. In summary, in order to find the best available precision given a set of timestamps (collected over a

single holdover window), we vary t_{bin} and t_{Acq} until both the following conditions are satisfied:

$$\text{SNR} \geqslant \text{SNR}_{\text{th}}, \tag{C1}$$

$$C(\tau^{\text{max}}) \geqslant N_{\text{min}}. \tag{C2}$$

Working at a suboptimal SNR still allows us to find the offset because even though we see multiple peaks ($t_{\text{Acq}} > \kappa t_{\text{bin}}$), all such peaks are above the average noise level. Since the range rate change can be calculated looking at the width of the peak and knowledge of acquisition time, the true offset can then be determined. The precision achievable if we work in this suboptimal SNR regime (and require N_{min} number of ebits to be collected on average within t_{Acq}) is given by

$$t_{\text{bin}} = \text{SNR}_{\text{th}}^2 \frac{N_{\text{min}}}{R \eta^2} \left(1 + \frac{R_{\text{bkg}}}{R \eta}\right). \tag{C3}$$

In Fig. 15 we show that this precision is higher than what is achievable if we work only in the max SNR regime. Working in this regime can be especially useful for low source rate or high loss or slightly oblique pass (high relative velocity) scenarios. Also, for comparison we show a scenario where the max SNR is less than the threshold SNR and thus no working precision can be obtained.

APPENDIX D: EFFECT OF DETECTOR JITTER ON SIGNAL-TO-NOISE RATIO AND ACHIEVABLE PRECISION

Let us say that the detector jitter accounts for a uncertainty σ_j (standard deviation) in the timestamps of the detected photons. This leads to a peak broadening effect adding onto the effect of range-rate change. Therefore, a smaller maximum

precision is now achievable, other factors remaining the same (see Fig. 16). Appending Eq. (25) for the effects of jitter, we find that this reduced precision is given by

$$t_{\text{bin}} \geqslant \frac{N_{\text{min}}}{R \eta \mathcal{K}} + \sigma_j. \tag{D1}$$

The above equation can also be understood by realizing that, since the jitter already leads to a peak broadening by the amount σ_j, the peak broadening effect due to range-rate change tolerable at a given working precision t_{bin} is smaller. This leads to a smaller t_{Acq}^{opt} and is given by $\kappa(t_{\text{bin}} - \sigma_j)$. This has implications for the SNR of the correlation function peaks as well. Since the optimal acquisition time is now reduced to $\kappa(t_{\text{bin}} - \sigma_j)$, the max SNR achievable becomes

$$\text{SNR}_{\text{max}} \approx \sqrt{\frac{\eta \kappa}{t_{\text{bin}}\left(1 + R_{\text{bkg}}/R\eta\right)}} \left(1 - \frac{\sigma_j}{t_{\text{bin}}}\right), \tag{D2}$$

which is meaningful only when $t_{\text{bin}} > \sigma_j$. This reduces to the jitterless case for $\sigma_j = 0$. In the limiting case of $\sigma_j = t_{\text{bin}}$ shows than $\text{SNR} = 0$, i.e., no peak can be seen at the working precision of t_{bin}. Furthermore, contrary to the jitterless case, here the SNR is not independent of the precision t_{bin}. Thus, imposing a threshold condition on the required SNR [analogous to Eq. (23)], and then solving the equation for t_{bin}, gives a relation for the maximum achievable precision in terms of the imposed threshold SMR_{th}. This is given by

$$t_{\text{bin}} \geqslant \frac{\sigma_j}{1 - \frac{S_{th}^2}{\eta \kappa}\left(1 + \frac{R_{\text{bkg}}}{R\eta}\right)}. \tag{D3}$$

[1] S. Haldar, I. Agullo, A. J. Brady, A. Lamas-Linares, W. C. Proctor, and J. E. Troupe, Towards global time distribution via satellite-based sources of entangled photons, Phys. Rev. A **107**, 022615 (2023).

[2] A. Lamas-Linares and J. Troupe, Secure quantum clock synchronization, in *Advances in Photonics of Quantum Computing, Memory, and Communication XI*, edited by Z. U. Hasan, P. R. Hemmer, A. E. Craig, and A. L. Migdall, International Society for Optics and Photonics, Vol. 10547 (SPIE, 2018), p. 105470L.

[3] J. Lee, L. Shen, A. Cerè, J. Troupe, A. Lamas-Linares, and C. Kurtsiefer, Symmetrical clock synchronization with time-correlated photon pairs, Appl. Phys. Lett. **114**, 101102 (2019).

[4] C. Spiess, S. Töpfer, S. Sharma, A. Kržič, M. C. Ponce, U. Chandrashekara, N. L. Döll, D. Rieländer, and F. Steinlechner, Clock synchronization with correlated photons, arXiv:2108.13466.

[5] J. S. Sidhu, S. K. Joshi, M. Gündogan, T. Brougham, D. Lowndes, L. Mazzarella, M. Krutzik, S. Mohapatra1, D. Dequal, G. Vallone, P. Villoresi, A. Ling, T. Jennewein, M. Mohageg, J. Rarity, I. F. amd Stefano Pirandola, and D. K. L. Oi, Advances in space quantum communications, IET Quantum Commun. **2**, 182 (2021).

[6] S. Khatri, A. J. Brady, R. A. Desporte, M. P. Bart, and J. P. Dowling, Spooky action at a global distance: Analysis of space-based entanglement distribution for the quantum internet, npj Quantum Inf. **7**, 4 (2021).

[7] W. F. McGrew, X. Zhang, R. J. Fasano, S. A. Schäffer, K. Beloy, D. Nicolodi, R. C. Brown, N. Hinkley, G. Milani, M. Schioppo, T. H. Yoon, and A. D. Ludlow, Atomic clock performance enabling geodesy below the centimetre level, Nature (London) **564**, 87 (2018).

[8] A. C. O'Connor, M. P. Gallaher, K. Clark-Sutton, D. Lapidus, Z. T. Oliver, T. J. Scott, D. W. Wood, M. A. Gonzalez, E. G. Brown, and J. Fletcher, Economic benefits of the global positioning system (GPS), Report sponsored by the National Institute of Standards and Technology (2019).

[9] M. D. Lachmann, H. Ahlers, D. Becker, A. N. Dinkelaker, J. Grosse, O. Hellmig, H. Müntinga, V. Schkolnik, S. T. Seidel, T. Wendrich, A. Wenzlawski, B. Carrick, N. Gaaloul, D. Lüdtke, C. Braxmaier, W. Ertmer, M. Krutzik, C. Lämmerzahl, A. Peters, W. P. Schleich *et al.*, Ultracold atom interferometry in space, Nat. Commun. **12**, 1317 (2021).

[10] IEEE Standard for a precision clock synchronization protocol for networked measurement and control systems, in *IEEE Std 1588-2008 (Revision of IEEE Std 1588-2002)* (IEEE, 2008), pp. 1–269.

[11] J. Troupe, S. Haldar, I. Agullo, and P. Kwiat, Quantum clock synchronization for future NASA deep space quantum links and fundamental science, arXiv:2209.15122.

[12] S. Bush, W. Challener, and G. Mantelet, A perspective on industrial quantum networks, AVS Quantum Sci. **3**, 030501 (2021).

[13] H. Bergeron, L. C. Sinclair, W. C. Swann, I. Khader, K. C. Cossel, M. Cermak, J.-D. Deschênes, and N. R. Newbury, Femtosecond time synchronization of optical clocks off of a flying quadcopter, Nat. Commun. **10**, 1819 (2019).

[14] P. Delva, F. Meynadier, C. Le Poncin-Lafitte, P. Laurent, and P. Wolf, Time and frequency transfer with a microwave link in the ACES/PHARAO mission, in *2012 European Frequency and Time Forum* (IEEE, 2012), pp. 28–35.

[15] J.-D. Deschênes, L. C. Sinclair, F. R. Giorgetta, W. C. Swann, E. Baumann, H. Bergeron, M. Cermak, I. Coddington, and N. R. Newbury, Synchronization of distant optical clocks at the femtosecond level, Phys. Rev. X **6**, 021016 (2016).

[16] J. Yin, Y.-H. Li, S.-K. Liao, M. Yang, Y. Cao, L. Zhang, J.-G. Ren, W.-Q. Cai, W.-Y. Liu, S.-L. Li, R. Shu, Y.-M. Huang, L. Deng, L. Li, Q. Zhang, N.-L. Liu, Y.-A. Chen, C.-Y. Lu, X.-B. Wang, F. Xu *et al.*, Entanglement-based secure quantum cryptography over 1,120 kilometres, Nature (London) **582**, 501 (2020).

[17] J. S. Sidhu, T. Brougham, D. McArthur, R. G. Pousa, and D. K. L. Oi, Finite key effects in satellite quantum key distribution, npj Quantum Inf. **8**, 18 (2022).

[18] G. M. Tino, A. Bassi, G. Bianco, K. Bongs, P. Bouyer, L. Cacciapuoti, S. Capozziello, X. Chen, M. L. Chiofalo, A. Derevianko, W. Ertmer, N. Gaaloul, P. Gill, P. W. Graham, J. M. Hogan, L. Iess, M. A. Kasevich, H. Katori, C. Klempt, X. Lu *et al.*, SAGE: A proposal for a space atomic gravity explorer, Eur. Phys. J. D **73**, 228 (2019).

[19] A. J. Brady and S. Haldar, Frame dragging and the Hong-Ou-Mandel dip: Gravitational effects in multiphoton interference, Phys. Rev. Res. **3**, 023024 (2021).

[20] M. Rivera-Tapia, A. Delgado, and G. Rubilar, Weak gravitational field effects on large-scale optical interferometric Bell tests, Classical Quantum Gravity **37**, 195001 (2020).

[21] D. R. Terno, F. Vedovato, M. Schiavon, A. R. H. Smith, P. Magnani, G. Vallone, and P. Villoresi, Proposal for an optical test of the Einstein equivalence principle, arXiv:1811.04835.

[22] D. Rideout, T. Jennewein, G. Amelino-Camelia, T. F. Demarie, B. L. Higgins, A. Kempf, A. Kent, R. Laflamme, X. Ma, R. B. Mann, E. Martin-Martinez, N. C. Menicucci, J. Moffat, C. Simon, R. Sorkin, L. Smolin, and D. R. Terno, Fundamental quantum optics experiments conceivable with satellites—reaching relativistic distances and velocities, Class. Quantum Grav. **29**, 224011 (2012).

[23] S. Wang, Symmetric private information retrieval supported by quantum-secure key-exchange network, Light Sci. Appl. **11**, 301 (2022).

[24] X. Xiang, B. Shi, R. Quan, Y. Liu, Z. Xia, H. Hong, T. Liu, J. Wu, J. Qiang, J. Jia, S. Zhang, and R. Dong, Quantum two-way time transfer over a hybrid free-space and fiber link, arXiv:2212.01741.

[25] R. Lafler and R. N. Lanning, Quantum time transfer for freespace quantum networking, arXiv:2211.00737.

[26] G.-J. Fan-Yuan, F.-Y. Lu, S. Wang, Z.-Q. Yin, D.-Y. He, Z. Zhou, J. Teng, W. Chen, G.-C. Guo, and Z.-F. Han, Measurement-device-independent quantum key distribution for nonstandalone networks, Photonics Res. **9**, 1881 (2021).

[27] G.-J. Fan-Yuan, F.-Y. Lu, S. Wang, Z.-Q. Yin, D.-Y. He, W. Chen, Z. Zhou, Z.-H. Wang, J. Teng, G.-C. Guo, and Z.-F. Han, Robust and adaptable quantum key distribution network without trusted nodes, Optica **9**, 812 (2022).

[28] J. Illiano, M. Caleffi, A. Manzalini, and A. S. Cacciapuoti, Quantum internet protocol stack: A comprehensive survey, Comput. Networks **213**, 109092 (2022).

[29] M. Caleffi, M. Amoretti, D. Ferrari, D. Cuomo, J. Illiano, A. Manzalini, and A. S. Cacciapuoti, Distributed quantum computing: A survey, arXiv:2212.10609.

[30] J.-G. Ren, P. Xu, H.-L. Yong, L. Zhang, S.-K. Liao, J. Yin, W.-Y. Liu, W.-Q. Cai, M. Yang, L. Li, K.-X. Yang, X. Han, Y.-Q. Yao, J. Li, H.-Y. Wu, S. Wan, L. Liu, D.-Q. Liu, Y.-W. Kuang, Z.-P. He *et al.*, Ground-to-satellite quantum teleportation, Nature (London) **549**, 70 (2017).

[31] H. Dai, Q. Shen, C.-Z. Wang, S.-L. Li, W.-Y. Liu, W.-Q. Cai, S.-K. Liao, J.-G. Ren, J. Yin, Y.-A. Chen, Q. Zhang, F. Xu, C.-Z. Peng, and J.-W. Pan, Towards satellite-based quantum-secure time transfer, Nat. Phys. **16**, 848 (2020).

[32] A. Villar, A. Lohrmann, X. Bai, T. Vergoossen, R. Bedington, C. Perumangatt, H. Y. Lim, T. Islam, A. Reezwana, Z. Tang, R. Chandrasekara, S. Sachidananda, K. Durak, C. F. Wildfeuer, D. Griffin, D. K. L. Oi, and A. Ling, Entanglement demonstration on board a nano-satellite, Optica **7**, 734 (2020).

[33] California-Polytechnic-State University, CubeSat Design Specification Revision 14, https://www.cubesat.org/cds-announcement.

[34] D. K. L. Oi, A. Ling, G. Vallone, P. Villoresi, S. Greenland, E. Kerr, M. Macdonald, H. Weinfurter, H. Kuiper, E. Charbon, and R. Ursin, Cubesat quantum communications mission, EPJ Quantum Technol. **4**, 6 (2017).

[35] S. Dolinar, K. M. Birnbaum, B. I. Erkmen, and B. Moision, On approaching the ultimate limits of photon-efficient and bandwidth-efficient optical communication, in *2011 International Conference on Space Optical Systems and Applications (ICSOS)* (IEEE, 2011), pp. 269–278.

[36] M. T. Taylor, A. Belmonte, L. Hollberg, and J. M. Kahn, Effect of atmospheric turbulence on timing instability for partially reciprocal two-way optical time transfer links, Phys. Rev. A **101**, 033843 (2020).

[37] C. Ho, A. Lamas-Linares, and C. Kurtsiefer, Clock synchronization by remote detection of correlated photon pairs, New J. Phys. **11**, 045011 (2009).

[38] S. Y. Zhu and E. Groten, Relativistic effects in GPS, in *GPS-Techniques Applied to Geodesy and Surveying*, edited by E. Groten and E. Strauß, Lecture Notes in Earth Sciences, Vol. 19 (Springer-Verlag, Berlin, Heidelberg, 1988), p. 41.